nature reviews physics

https://doi.org/10.1038/s42254-024-00775-4

Technical review

Check for updates

Nanoscale diamond quantum sensors for many-body physics

Jared Rovny[1], Sarang Gopalakrishnan[1], Ania C. Bleszynski Jayich[2], Patrick Maletinsky[3], Eugene Demler[4] & Nathalie P. de Leon[1]

Abstract

Nitrogen vacancy (NV) centre quantum sensors provide unique opportunities in studying condensed matter systems, as they are quantitative, non-invasive, physically robust, offer nanoscale resolution and may be used across a wide range of temperatures. These properties have been exploited in recent years to obtain nanoscale resolution measurements of static magnetic fields arising from spin order and current flow in condensed matter systems. Compared with other nanoscale magnetic-field sensors, NV centres have the advantage that they can probe quantities that go beyond average magnetic fields. Leveraging techniques from magnetic resonance, NV centres can perform high-precision noise sensing and have given access to diverse systems, such as fluctuating electrical currents in simple metals and graphene, as well as magnetic dynamics in yttrium iron garnet. In this Technical Review, we provide an overview of NV sensing platforms and modalities and discuss the connections between specific NV measurements and important physical characteristics in condensed matter, such as correlation functions and order parameters, that are inaccessible by other techniques. We conclude with our perspectives on the new insights that may be opened up by NV sensing in condensed matter.

Sections

[1]Department of Electrical and Computer Engineering, Princeton University, Princeton, NJ, USA. [2]Department of Physics, University of California Santa Barbara, Santa Barbara, CA, USA. [3]Department of Physics, University of Basel, Basel, Switzerland. [4]Institute for Theoretical Physics, ETH Zurich, Zurich, Switzerland. e-mail: npdeleon@princeton.edu

Key points

- Nitrogen vacancy (NV) centres can probe static and dynamic fields in a momentum-resolved and frequency-resolved way across a wide range of temperatures, from cryogenic temperatures to 1,000 K, complementing existing nanoscale probes.
- Static fields can be quantitatively mapped with nanotesla sensitivity and nanometre spatial resolution using NV centres, diagnosing microscopic properties in magnetic materials, transport systems and superconductors, as well as in diamond anvil cells under extreme gigapascal pressures.
- NV centres can also be used to measure noise from dynamic systems in a tunable way, providing access to the spectral density of noise from DC to tens of gigahertz while using the NV-sample distance to probe the relevant length scales of system dynamics.
- Recent progress has been made in coherent NV-based noise measurements, in which measurements resolving transitions in the shape of the NV coherence decay or simultaneous measurements of many NV centres can provide new windows into dynamic systems.

Introduction

Much of what we know about condensed matter systems — their structure, excitations and dynamics — is inferred from bulk transport and spectroscopy. These techniques can be useful for inferring fundamental properties such as how excitations disperse, probing momentum-resolved spectra from large samples and optically probing low-momentum spectra from 2D samples. However, spatially averaged probes such as transport, neutron scattering or angle-resolved photoemission spectroscopy can provide incomplete or misleading data in non-uniform samples[1], in which the sample is disordered or has interactions that give it a local tendency to phase-separate[2], inducing the spontaneous formation of static or fluctuating domains[3]. Thus, quantitatively understanding such phenomena requires local, momentum-resolved probes. There are several established nanoscale probes that are useful for local studies of samples. Notably, scanning-tunnelling microscopy (STM) measures the local electronic density of states[4–6], microwave impedance microscopy measures local conductivity and permittivity[7] and scanning magnetometry techniques such as scanning superconducting quantum interference device (SQUID) microscopy[8] and magnetic force microscopy (MFM) measure local magnetic fields[9]. Each probe carries advantages and tradeoffs. Taking two examples, scanning SQUID magnetometers offer extremely high sensitivity (down to a few nT $Hz^{-1/2}$), but must operate at low temperature (typically below 10 K) and have worse sensitivity at higher spatial resolution; and STM offers extremely high (angstrom-scale) spatial resolution, but typically requires clean conducting surfaces and cannot report on local magnetic fields and dynamics.

Over the past decade, nitrogen vacancy (NV) centres in diamond have emerged as a new class of nanoscale sensors that complement these technologies in their temperature range and in their ability to probe both static and dynamic properties in a momentum-resolved and frequency-resolved way[10–12]. NV magnetometry offers a combination of nanometre spatial resolution and nanotesla sensitivity in magnetic imaging[13], together with a wide operational range in temperature, magnetic field or pressure. NV centres have been employed to measure static local fields from antiferromagnetic order[14,15], multiferroic[16] order and from currents in materials with electron hydrodynamics[17,18] and superconductivity[19–22], as well as linear dynamics in contexts such as magnon imaging[23,24] and conductivity imaging[25]. Recently, NV centres have been used to probe out-of-equilibrium systems, such as a magnon scattering platform[26] and electron–phonon instability in graphene[27]. In these dynamic systems, newly developed NV centre sensing methods such as covariance magnetometry[28] and gaining access to the noise correlation time via coherence decay[29–31] may provide insights that are difficult to access with other sensing techniques.

An NV centre is a point defect in diamond consisting of a substitutional nitrogen next to a vacancy in the lattice. Effectively, it works as an optically addressable qubit that can sense its environment with extremely high spatial resolution[32–34]. The spatial resolution is determined by the offset between the NV centre and the material of interest (typically 5–100 nm), ultimately limited by the extent of the electronic wavefunction (around 1 nm). Because the NV centre offers both local resolution and the entire suite of qubit-manipulation techniques developed in the context of nuclear magnetic resonance[35], it enables a host of new local sensing technologies. As an example of how versatile these probes are, they can be used to measure static magnetic fields through a shift of the qubit frequency[32,36], to measure the noise spectral density at the qubit transition frequency as the noise can change the qubit's T_1 time[25,37,38] and to measure dynamic structure such as the spatiotemporal correlations of the noise in an underlying sample, which can be detected in a coherent (T_2-limited) measurement of multiple NV centres[28]. Furthermore, beyond high-sensitivity magnetometry, NV centres are also able to report on electric fields, temperature and strain, useful, for instance, in high-pressure diamond anvil cell (DAC) experiments[39–43].

The momentum resolution of an NV centre comes from changing its distance from the sample and requires the distance between the NV centre and the sample to be measured[12]. Notably, the momentum-resolved current noise that NV centres measure goes beyond what one can measure using techniques such as neutron scattering. Probes such as neutron scattering[44], X-ray scattering[45] and electron energy loss spectroscopy[46] measure the momentum-dependent density response, from which one can extract the behaviour of longitudinal currents (those along the wavevector being probed) but not transverse ones. The current noise that an NV centre detects can also be sensitive to transverse current fluctuations and can, therefore, pick up the response of the electron fluid to being sheared; the shear response is a key diagnostic of Wigner crystallization[47], as well as a natural probe of viscous hydrodynamic behaviour[48,49]. Furthermore, although neutron scattering averages over the bulk of the material, NV centres enable real-space probing with nanoscale resolution, giving access to spatially inhomogeneous momentum information.

This Technical Review outlines the physics of NV centres as it relates to condensed-matter sensing experiments and illustrates a few recent developments and proposals in this area. For an in-depth review comparing NV magnetometry with other magnetic microscopy techniques including X-ray and magneto-optical spectroscopy, the reader is referred to refs. 8,34,50. Here, we focus on the parametrization of different NV centre sensing modalities in terms of physical quantities of interest for condensed matter physics and review the current state of the art, including new sensing techniques and sophisticated methods in image reconstruction, efficient sampling and sensitivity enhancement. We conclude with a discussion of new opportunities

in condensed matter sensing that are enabled by this unique probe and toolkit.

Principles of NV centre sensing

The ground state electronic configuration of an NV centre has spin $S = 1$. The ground state spin can be initialized and measured even at room temperature, with spin coherence times up to a few milliseconds[36], and at cryogenic temperatures with coherence times exceeding 1 s (ref. 51). The long spin coherence time is enabled by weak spin–orbit coupling, low electron–phonon coupling and a quiet spin environment in ultrapure diamond[52]. An NV centre can be used as a sensor over a wide range of parameters, from cryogenic temperatures to nearly 1,000 K (refs. 53,54) and from vacuum to gigapascal pressures[39,40], largely because its electronic level structure allows for non-resonant optical initialization and readout and because its structure in diamond is exceptionally robust.

An NV centre measurement typically consists of three steps: initialization by optical polarization into the $|m_s = 0\rangle$ spin state, interaction with external fields using a tailored sensing modality and optical detection through spin-dependent fluorescence (Fig. 1a). There are three broad sensing modalities, covering characteristic frequency ranges from DC to ~100 GHz (Box 1). First, optically detected magnetic resonance (ODMR) spectroscopy of the $|m_s = 0\rangle \rightarrow |m_s = \pm 1\rangle$ transition frequency enables DC magnetic field sensing. Second, coherent Ramsey-based protocols may incorporate frequency-selective pulse sequences for AC sensing up to ~10 MHz frequencies. Third, relaxometry measures fields fluctuating at the NV transition frequency by monitoring the NV centre decay rate Γ among the ground state spin levels. Relaxometry and ODMR have been demonstrated up to ~200 GHz (ref. 55), in which the attainable frequency is determined by the strength of the external magnetic field and the availability of microwave (MW) hardware used to drive the NV centre spin transitions.

Sensing platforms

Typically, NV centres are deployed in three broad categories of platforms. The most common measurements are performed in bulk diamond, using NV centres that are either sparse and optically resolvable (Fig. 1b) or dense to produce large ensembles that enable millimetre-scale imaging[56] (Fig. 1c). In recent years, diamond fabrication and processing have seen substantial advances, including high collection efficiency scanning tips[57,58] (Fig. 1d) and nanoscale structures (Fig. 1e) such as 'smart-cut' nanoscale diamond membranes[59,60] that can be deposited onto target samples.

Each of these platforms has inherent benefits and tradeoffs. Measurements in bulk diamond are the most convenient, in which coherent NV centres can be reliably prepared a few nanometres below the diamond surface[61], but optical access and collection efficiency can be problematic in the presence of a sensing target. Ensemble measurements provide high sensitivity and surface coverage at the cost of spatial resolution, but spin–spin interactions place an upper bound on the useful NV centre density; however, dynamical decoupling protocols tailored to the spin environment can effectively suppress these interactions[62]. Measurements using NV centres embedded into an atomic force microscopy-style scanning tip provide nanometre scanning resolution, but are slow as the tip must raster scan over a sample, and the incorporated NV centres are typically stood off from the sample by tens of nanometres. Finally, diamond nanostructures and membranes can be incorporated directly onto pre-fabricated target samples in a way that provides high collection efficiency and close NV-sample proximity; however, nanostructures can be challenging to reliably fabricate, manipulate and place precisely on the target. In many cases, a system of interest may be measured using multiple modalities to paint a more complete picture of its properties[63].

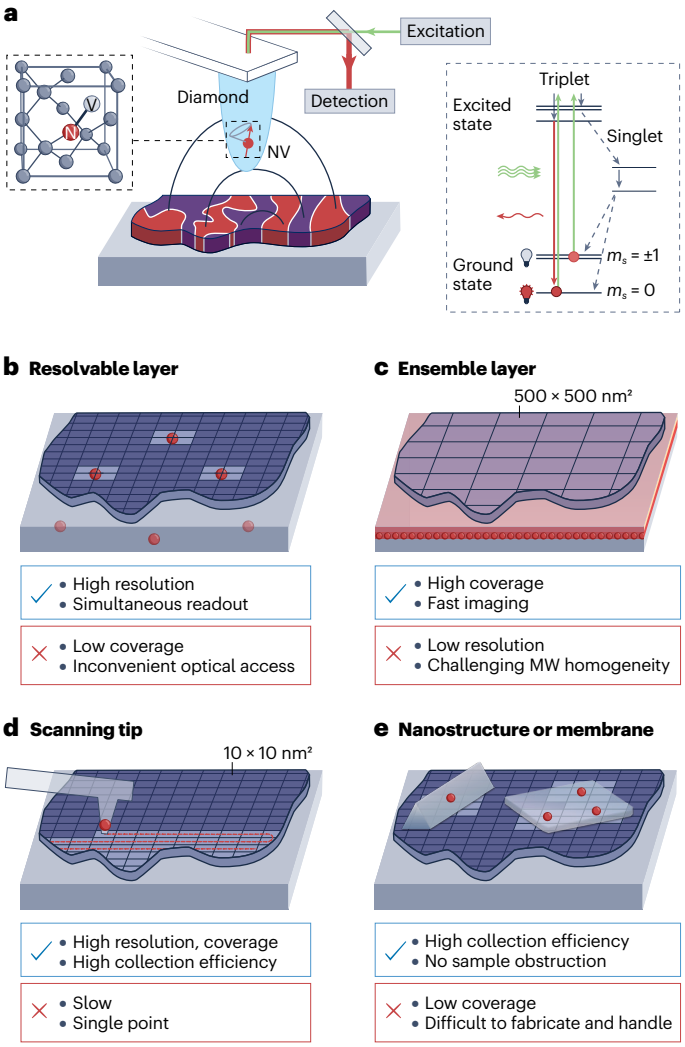

Fig. 1 | Nitrogen vacancy sensing platforms. a, A nitrogen vacancy (NV) centre in diamond detects local fields from a target system with nanometre resolution. Off-resonant excitation light is used to spin polarize the NV centre and subsequently read out its state through spin-dependent fluorescence. **b**–**e**, Different NV sensing platforms with their pros and cons. In all cases, defects are incorporated in the diamond either during growth or using ion implantation after growth. Bulk diamond substrates, either with resolvable NV centres (part **b**) or dense ensembles of NV centres (part **c**), are most common and are readily prepared. **d**, Scanning atomic force microscopy-style tips with embedded NV centres provide nanometre-scale spatial resolution, which is much better than micron-scale ensemble imaging resolution, although experiments are much slower. **e**, Although diamond fabrication and subsequent micro-manipulation are challenging, nanoscale diamond structures including nanodiamonds, beams, pillars and membranes are versatile and can be placed directly on a target sample, providing close target proximity, easy optical access and higher collection efficiency.

Box 1 | Nitrogen vacancy centre sensing modalities

The typical nitrogen vacancy (NV) centre Hamiltonian has the form

$$\hat{H}_{NV} = \mathcal{A}\hat{S}_z^2 + \mathcal{B}\hat{S}_z + \mathcal{C}(\hat{S}_y^2 - \hat{S}_x^2) + \mathcal{D}(\hat{S}_x\hat{S}_y + \hat{S}_y\hat{S}_x), \quad (4)$$

in which (for small applied fields) the separate contributions cause shifting ($\mathcal{A}$) and splitting ($\mathcal{B}$, $\mathcal{C}$, $\mathcal{D}$) of the $|m_s = \pm 1\rangle$ states according to the energy diagram in panel **a** of the figure, which describes the approximate couplings to parallel and perpendicular magnetic fields (B), electric fields (E), stress (σ) and temperature (T); note that these sensitivities may change depending on, for example, temperature and field orientation[53,204,217]. Continuous wave optically detected magnetic resonance provides a simple and robust method for spectroscopy of the Hamiltonian in equation (4), but is insensitive to AC fields and has limited sensitivity to DC fields.

Pulsed Ramsey-type protocols (see the figure, panel **b**) employ trains of pulses to modulate the NV centre in the time domain, making the NV centre sensitive to a band of frequencies centred at the pulsing rate. Pulsed methods are extremely versatile and are routinely used for frequency-selective spectroscopy and to considerably improve measurement sensitivity, including sensitivity to DC fields through lock-in gradiometry[78]. Incoherent relaxometry (see the figure, panel **c**), although less versatile, provides access to high-frequency fields inducing single-quantum ($|m_s = \pm 1\rangle \rightarrow |m_s = 0\rangle$) and double-quantum ($|m_s = \pm 1\rangle \rightarrow |m_s = \mp 1\rangle$) transitions of the NV centre, where this distinction can be useful in diagnosing whether the relaxing fields are electric or magnetic in nature[218]. Beyond the simplified Hamiltonian in equation (4), it is often advantageous to intentionally mix spin states or probe dressed levels of a driven state[204].

Approximate frequency ranges and length scales accessible through common NV centre sensing modalities are given in panel **d** of the figure, in which the length scales refer to the NV-sample distance (or the square root of areal sensing resolution for ensembles). The approximate optimal sensitivities are shown in each region and assume either the minimum detectable field using coherent T_2 sensing (η_B) or the minimum detectable mean square noise amplitude in a 1 Hz band using incoherent T_1 relaxometry (η_S). Coherent (T_2) sensing is typically performed below 100 MHz, limited by the pulse rate, and has a sensitivity limited by the NV centre T_2 time, which degrades for shallow NV centres. Incoherent (T_1) noise spectroscopy has been demonstrated up to hundreds of gigahertz and has a sensitivity limited by the NV centre T_1 time, which is longer than T_2. For both T_2 and T_1 magnetometry, the sensitivity can be improved at the cost of resolution by using NV centre ensembles, as the sensitivity improves with $\sqrt{N}$ for N NV centres; however, dense ensembles typically incur other penalties, such as shorter coherence times, owing to the high defect density. Selected NV centre experiments are also indicated, in which achieved sensitivities vary. At DC, comparisons are also made with nanowire MFM (nw-MFM) and scanning superconducting quantum interference device (SS) measurements[34]. The approximate length scale and timescale of system excitations accessible to neutron scattering and optical pump/probe experiments are also shown for context. Although these descriptions provide a rough overview of the NV sensing landscape, note that they are simplified, as they omit sensing permutations such as shallow NV ensembles and T_2 noise spectroscopy.

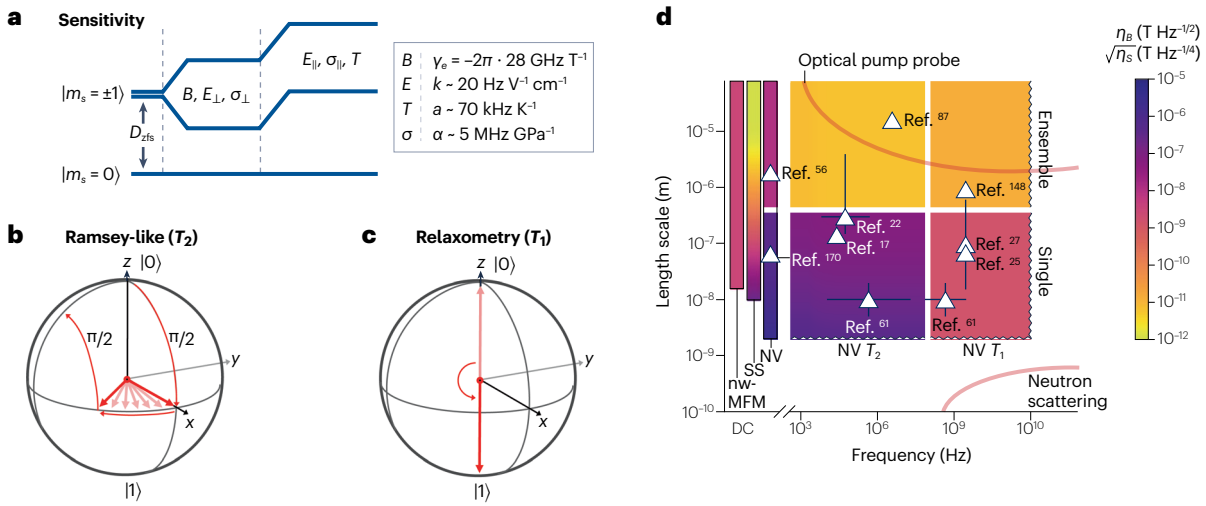

Proximity to the surface is crucial for spatial resolution, as an NV centre at distance d from the surface is sensitive to stray fields originating from a region on the surface with spatial extent proportional to d (Box 2). However, close NV-sample proximity, enabled by very shallow ion implantation just a few nanometres from the diamond surface and subsequent fabrication[64,65], incurs decoherence owing to surface noise and charge state instabilities owing to surface electronic traps. Both coherence times and charge state stability have been considerably improved through a better understanding of surface noise sources and treatment[61,66–68], although achieving bulk-like properties near the surface remains an open challenge[69]. Improving sensitivity in a given experiment requires a judicious choice of sample-NV distance versus coherence time, number of NV centres and the readout method (which can also feature

tradeoffs, for instance, sacrificing speed for higher fidelity when using spin-to-charge conversion)[70–74].

NV centre sensitivity

Although NV centres are most often used to detect magnetic fields B through the induced Zeeman splitting frequency $\omega = D_{zfs} \pm \gamma_e B$, in which the zero field splitting is $D_{zfs} = 2\pi \times 2.87$ GHz and the electron gyromagnetic ratio is $\gamma_e = -2\pi \times 28.02$ GHz T^{-1}, they may also be used to detect electric fields, temperature and strain. An important advantage offered by NV centres over nanoSQUIDs, MFM or STM is the ability to engineer their sensitivity to the environment through pulse sequences designed to select certain frequencies[75] or physical observables[39].

The sensitivity of an NV centre measurement may be boosted by increasing the number of NV centres, extending the coherence time, improving the readout fidelity (through techniques such as

Box 2 | Dynamical correlators from nitrogen vacancy noise spectroscopy

Nitrogen vacancy (NV) relaxation and decoherence times can be explicitly related to the field noise at the NV centre and thus to the physical autocorrelation functions of the noise source. To keep the discussion here concrete, we focus on magnetic field noise at the NV centre owing to classical magnetic or current noise in the sample: $\hat{H}_{NV} = D_{zfs}\hat{S}_a^2 - \gamma_e B_0 \hat{S}_a - \gamma_e \mathbf{B}(t)\cdot\hat{\mathbf{S}}$, in which $\hat{S}_i$ are spin-1 operators, B_0 is a static external field and we define $\omega_0 = D_{zfs} \pm \gamma_e B_0$. Here we have defined coordinate axes a, b, c such that unit vector $\hat{\mathbf{a}}$ points along the NV quantization axis and unit vectors $\hat{\mathbf{b}}$, $\hat{\mathbf{c}}$ are perpendicular to it. For a relaxometry experiment measuring the total decay rate T_1^{-1} out of $m_s = 0$ (which is three times faster than the individual transition rates from 0 to +1 or −1 alone)[94,218], Fermi's golden rule implies

$$T_1^{-1} = \frac{3}{2}\gamma_e^2 S_B^{\perp}(\omega_0), \quad S_B^{\perp}(\omega) = \int \mathrm{d}t\, e^{-i\omega t}\langle B_+(t)B_-(0)\rangle, \quad B_\pm = B_b \pm iB_c, \quad (5)$$

in which the NV centre transition frequency ω_0 determines the detected frequency (usually a few gigahertz) and in which the factor of 1/2 results from the transition matrix elements.

For dynamical-decoupling-based T_2 spectroscopy, it is instead more natural to model the NV centre decoherence as a stretched exponential $C(t) = \exp[-(t/T_2)^p]$, in which p is the stretching factor. Then, under dynamical decoupling using N equally spaced pulses with interpulse spacing τ and total time $T = N\tau$:

$$T_2^{-p} = \frac{\gamma_e^2}{\pi T^p}\int_0^\infty \mathrm{d}\omega S_B^{\parallel}(\omega)\frac{F_N(\omega\tau)}{\omega^2}, \quad S_B^{\parallel}(\omega) = \int \mathrm{d}t\, e^{-i\omega t}\langle B_a(t)B_a(0)\rangle, \quad (6)$$

in which the detected noise frequency is set by the pulse rate τ^{-1} (typically less than 100 MHz) through the pulse sequence filter function $F_N(\omega\tau) = 8\sin^4(\omega\tau/4)\sin^2(N\omega\tau/2)\cos^{-2}(\omega\tau/2)$. For large N, this is sharply peaked at $\omega = \pi/\tau$, and it is common to approximate the spectral density as $S_B^{\parallel}(\pi/\tau) = -\pi\ln[C(T)]/T$ (refs. 61,83,218), in which $C(t)$ is the decoherence function defined earlier.

It remains to calculate the noise spectrum $S_B(\omega)$ at the NV centre from a given source, which will depend on the sample and geometry. As an example, we consider relaxometry in the presence of classical current noise in the sample[219]. The sample is taken to lie in the xy plane and the NV centre is displaced by d along the z-axis, aligned along axis $\hat{\mathbf{a}}$ (see the figure). The areal current $\mathbf{J}(\mathbf{r}, t)$ at a point $\mathbf{r}$ in the sample is a classical field that fluctuates slowly enough that its effect on the NV centre can be treated as instantaneous (this 'quasistatic' assumption always holds in practice). In this case, the NV centre experiences a fluctuating magnetic field that can be related to the current profile through the Biot–Savart law:

$$\mathbf{B}(t) = \frac{\mu_0}{4\pi}\int \mathrm{d}^2\mathbf{r}\,\frac{\mathbf{J}(\mathbf{r}, t)\times(\hat{\mathbf{z}}d - \mathbf{r})}{|r^2 + d^2|^{3/2}}. \quad (7)$$

Thus, equations (5) and (7) relate the NV centre relaxation time to the current autocorrelation tensor $\langle J_i(\mathbf{x}, t)\, J_j(\mathbf{0}, 0)\rangle$ and a spatial smoothing factor from the distance dependence. Next, the fluctuation-dissipation theorem (FDT) relates the current autocorrelation function to the current response function, $\chi_{ij}(q, \omega)$, which will depend on the conductivity $\sigma_{ij}(q, \omega)$ (although the relation (7) is not precisely q-resolved, the d-dependence of T_1 imposes strong constraints on the q-dependence). For a 2D conductor at high temperatures such that $\coth(\hbar\omega_0/2k_BT) \approx 2k_BT/(\hbar\omega_0)$, the noise density is[48]

$$2S_B^{x,y}(\omega) = S_B^z(\omega) = \frac{\mu_0^2 k_B T}{16\pi}\varsigma(d, \omega),$$
$$\varsigma(d, \omega) = \frac{1}{d^2}\int_0^\infty dx\, x e^{-x}\mathrm{Re}[\sigma^{\mathrm{T}}(x/2d, \omega)], \quad (8)$$

in which $\sigma^{\mathrm{T}}(q, \omega)$ is the q-dependent transverse conductivity, which can be probed through the distance dependence of equation (8). Finally, assuming the NV centre axis $\hat{\mathbf{a}}$ makes angle θ with z, the relaxation rate is then $T_1^{-1} = \frac{3}{2}\gamma_e^2 S_B^z(\omega_0)(1 + \frac{1}{2}\sin^2(\theta))$ (ref. 25).

A similar procedure may be followed for other noise sources, such as magnetic fluctuations[139,148,220], or other geometries. For instance, diffusive transport in a conducting film of thickness a and conductivity $\sigma = \mathrm{Re}[\sigma(\omega_0)] \approx \sigma(0)$ produces noise according to equation (8) with distance dependence $\varsigma(d, \omega) = (d^{-1} + (d+a)^{-1})\sigma$, which scales as d^{-1} or d^{-2} for thick and thin films, respectively[25,37]. For noise originating from paramagnetic spins (such as nuclear spins), the distance dependence is instead d^{-6} from a single spin[221], d^{-4} from a 2D layer[163] or d^{-3} from a 3D half-space[222].

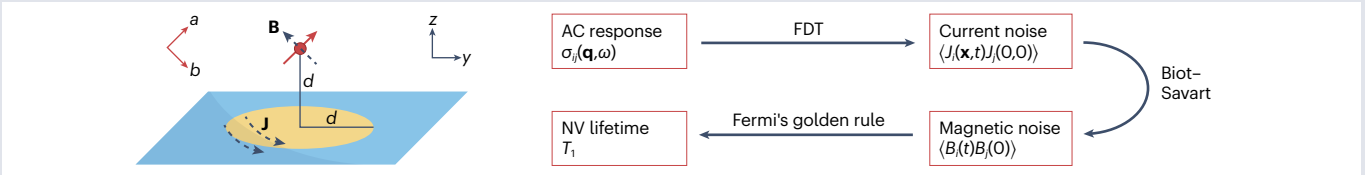

Table 1 | Demonstrated sensitivities of different nitrogen vacany centre sensing platforms, measured in bulk diamond unless indicated otherwise

	Deep NV centres	Shallow NV centres	Deep NV centre ensembles	Shallow NV centre ensembles
DC magnetic	72 nT $Hz^{-1/2}$[a,b] (ref. 36)	300 nT $Hz^{-1/2}$ (st) (ref. 99)	24.6 nT $Hz^{-1/2}$ $\mu m^{-3/2}$ (qdm)[a] (ref. 196); 11.5 nT $Hz^{-1/2}$ $\mu m^{-3/2}$ (ref. 197)	176 nT $Hz^{-1/2}$ $\mu m^{-3/2}$ (ref. 198); 1,440 nT $Hz^{-1/2}$ $\mu m^{-3/2}$ (dac) (ref. 39)
AC magnetic	4.3 nT $Hz^{-1/2}$[a] (ref. 36)	50 nT $Hz^{-1/2}$ (st) (ref. 79)	2.4 nT $Hz^{-1/2}$ $\mu m^{-3/2}$[a] (ref. 87); 5.3 nT $Hz^{-1/2}$ $\mu m^{-3/2}$ (ref. 197)	199,200
DC electric	89.1 mV μm^{-1} $Hz^{-1/2}$ (ref. 191)	3,520 mV μm^{-1} $Hz^{-1/2}$ (st) (ref. 201)	2,217 mV $Hz^{-1/2}$ $\mu m^{-\frac{5}{2}}$ (ref. 202)	–
AC electric	20.2 mV μm^{-1} $Hz^{-1/2}$ (ref. 191)	24–26 mV μm^{-1} $Hz^{-1/2}$ (st) (refs. 203,204)	11 mV $Hz^{-1/2}$ $\mu m^{-\frac{5}{2}a}$ (ref. 205)	–
Stress	–	0.6 MPa $Hz^{-1/2}$ (dac)[b] (ref. 193)	0.06 MPa $Hz^{-1/2}$ $\mu m^{-3/2}$ (qdm)[a] (ref. 206)	3.6 MPa $Hz^{-1/2}$ $\mu m^{-3/2}$ (dac) (ref. 39)
Temperature	5 mK $Hz^{-1/2}$[a] (ref. 192)	24 mK $Hz^{-1/2}$ (ref. 207)	194 mK $Hz^{-1/2}$ $\mu m^{-3/2}$ (ref. 208)	4.8 mK $Hz^{-1/2}$ $\mu m^{-3/2}$ (ref. 209)

Platforms include scanning tip (st), diamond anvil cell (dac), quantum diamond microscope (qdm), nanostructure/membrane (nsm) and nanodiamond (nd). Other structures, such as diamond-etched solid-immersion lenses, are not included here. Shallow nitrogen vacancy (NV) centres are within ~100 nm of the diamond surface. Volume-normalized sensitivities are reported for NV centre ensembles to capture realistic imperfections that can be expected in ensemble-implanted samples. For detailed temperature-dependent NV properties, see refs. 210–212. For detailed NV-density dependence, see refs. 213–215. For detailed depth dependence, see refs. 29,61,216. [a]Makes use of ^{12}C isotopically enriched diamond. [b]Derived using values from separate measurements[36,193].

spin-to-charge conversion[71] and repetitive readout using nuclear spin ancillae[70,76]) and, crucially for nanoscale sensing, decreasing the distance to the target. Typically achievable sensitivities are ~1 μT $Hz^{-1/2}$ at DC[77] and 50 nT $Hz^{-1/2}$ at AC[17,78,79] (Table 1). The single-NV spin projection noise limit to the sensitivity depends on the NV centre coherence time T_2 (ref. 32), which is fundamentally limited at room temperature by phonon-induced depolarization on the millisecond timescale and which may be much longer at low temperatures[51,80]. Spatial resolution down to ~20 nm has been achieved using scanning tips[81], whereas implantation into unstructured substrates allows for NV centres as close as 2–3 nm to the surface[82,83], which approaches the fundamental limit of ~1 nm imposed by the size of the NV defect wavefunction[84]. Furthermore, subdiffraction imaging techniques allow the NV centre to be laterally located to within a few nanometres[85,86].

Although the NV centre spin coherence time and resonance frequency naively imply approximately kilohertz linewidth and megahertz or gigahertz frequency ranges for Ramsey spectroscopy and relaxometry, respectively, several protocols have been developed to surpass these limits. For detecting coherent signals, the NV sensor may be reinitialized and detected many times within the coherence time of the signal, enabling sub-millihertz linewidths[87–89]. To broaden the accessible frequencies, recent demonstrations have shown that dressed states and frequency mixing may be used to fill in the frequency gap between Ramsey and relaxometry protocols to access ~100 MHz frequencies, provided that mixing fields with sufficiently high power and frequency are available[90–93], whereas auxiliary spins may be leveraged to access different frequencies while boosting sensitivity[94]. Techniques have also been developed to improve spatial resolution and imaging, by reconstructing the source magnetization from the stray field maps measured by the NV centre using machine-learning algorithms[95] (Fig. 2a).

Static fields

A key feature of NV magnetometry is that it provides quantitative mapping of the stray magnetic fields, enabling, for instance, the precise determination of the average areal magnetization of 2D materials. Doing this allows for the validation of model Hamiltonians proposed for systems under study or for assessing the quality and homogeneity of well-understood compounds. Such quantitative magnetometry is enabled by the fact that the NV centre gyromagnetic ratio γ_e is identical between NVs, which allows one to linearly map changes in magnetic field to a frequency reference, without the need for any additional calibration measurements. A direct, quantitative determination of the physical properties of samples under investigation always needs to be inferred from the measured stray field maps. Indeed, careful data analysis[11] or reverse propagation[95,96] (from the measurement plane to the source) allows for such quantitative extraction of physical parameters of samples of interest and for the tracking of their evolution with external quantities such as temperature or magnetic fields. It is worth noting that such reverse propagation is an under-constrained problem for which, in general, no unique solution exists[12,97]. This is illustrated by the example of the so-called flux closure states, which are spin textures that generate zero magnetic stray field, such as a ring with tangentially aligned spins. In many cases, however, reasonable assumptions can be made to overcome this limitation, for example, if known anisotropies exist in magnetic systems[98]. Helpful strategies to address the ill-posed nature of the inverse problem, and other issues, such as numerical instabilities and issues related to boundary conditions, have been discussed[12,95–97].

Quantitative determination of magnetization strength

The quantitative determination of magnetization strength of magnetic materials and its dependence on a range of parameters (such as temperature) is one of the most fundamental characteristics of any magnetic material. NV magnetometry allows for the precise, quantitative determination of magnetization strengths down to the nanoscale. It is worth noting that NV magnetometry is only strictly quantitative in the regime of weak magnetic fields ($\lesssim$10 mT), where the first-order response of the NV ODMR frequencies dominates the Zeeman shift of the NV centre spin levels, and transverse magnetic fields only play a negligible role.

Specific examples in which NV magnetometry has been put to use in this context include the determination of magnetization strengths in few layers of magnetically ordered van der Waals materials, down to the monolayer[98,99] (Fig. 2a), and uncompensated magnetic

moments in antiferromagnets that occur either in the bulk[100,101] or on the surface of magnetoelectric antiferromagnets[14,102]. More conventional thin-film magnets have also been examined in this regard[103], but are typically accessible via other experimental approaches as well. A notable extension of such studies is the determination of magnetization strengths in spin spirals of bulk multiferroics[104,105].

The relevance of these results relies on their quantitative character, which, together with the temperature or field dependence of magnetization, provide key insight into the theoretical understanding of these materials. As a further example, NV magnetometry might be highly suited to validate recent theoretical predictions regarding the nature and strength of surface magnetization in magnetoelectric antiferromagnets[106].

Magnetization distributions

Quantitative NV magnetometry further enables the disambiguation between different types of domain walls in magnetic materials, such as Bloch and Néel domain walls. The latter nomenclature describes how the order parameter in a magnetic system evolves across domain walls that separate two domains of homogeneous order parameter — for Bloch (Néel) walls, the evolution is described by a rotation around a vector that is orthogonal to (contained in) the domain wall. The identification of the nature of such domain walls is of crucial importance to understanding and characterizing the type of exchange interactions that contribute to stabilizing a given magnetic order[107], with the Dzyaloshinskii–Moriya interaction being the most prominent example. An experimental distinction between different types of domain walls was measured using NV magnetometry, in a study in which

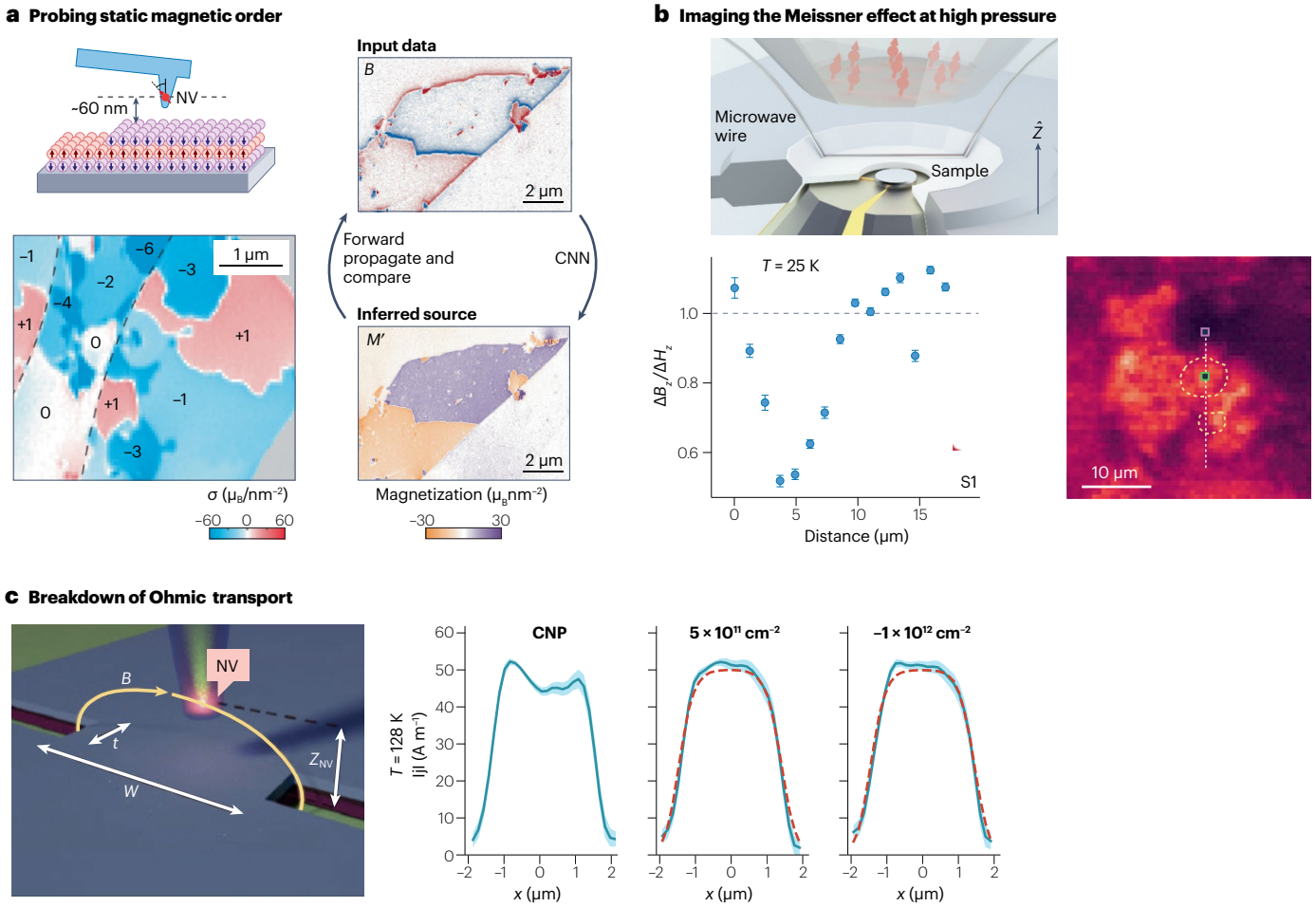

Fig. 2 | Imaging static fields with nitrogen vacancy centres. a, The left panels show a nitrogen vacancy (NV) centre scanning experiment measuring magnetic domains in a flake of CrI_3, revealing regions where the magnetization appears in integer multiples of the monolayer magnetization. To infer the source magnetization from the measured stray field maps (right panels), conventional linear inverse maps may be replaced by more robust convolutional neural networks (CNNs), which require no prior training and which use physics-informed forward propagation from the magnetisation map $\mathcal{M}'$ to the magnetic field map $\mathcal{B}$ at the measurement plane. **b**, Locally imaging the Meissner effect in CeH_9 at high pressure. The sample is compressed in a diamond anvil cell with an NV-containing layer in the upper diamond (top). Optically detected magnetic resonance measurements of the local magnetic field, taken along the linecut shown in the NV fluorescence image (bottom right), reveal inhomogeneities in diamagnetism at the micron scale (bottom left). **c**, Scanning NV magnetometry of the local electron flow profile through a constriction in graphene. The local current profile (right, carrier density indicated above each panel) shows characteristic Ohmic peaks at the charge neutrality point (CNP), which breaks down at low temperature away from CNP, indicating the absence of momentum-relaxing scattering as electron–electron scattering becomes more dominant. The bottom left part of panel **a** is reprinted with permission from ref. 98. The right part of panel **a** is adapted with permission from ref. 95. Panel **b** is adapted with permission from ref. 43. Panel **c** is adapted with permission from ref. 18.

thin films of the same magnetic material were subjected to different interfacial conditions[11]. Such analyses crucially depend on a proper characterization of the NV orientation and offset distance, the latter being the key parameter of concern. For reliable, quantitative conclusions, such characterizations are to be conducted in situ, on the sample under investigation, to avoid systematic errors and concurrent pitfalls in data analysis.

Furthermore, the study of topologically protected magnetic textures, such as magnetic skyrmions[108] and their winding numbers, is directly accessible and enabled by scanning NV magnetometry. Although a range of experimental techniques — including Lorentz transmission electron microscopy[109] and quantitative MFM[110] — have demonstrated direct, real-space imaging of skyrmions, scanning NV magnetometry[111–115] allows for quantitative imaging under ambient conditions and does not pose strong requirements on sample geometry or thickness. For example, skyrmion winding numbers on the level of individual skyrmions on a multilayer stack were determined in a sample under ambient conditions using static stray field imaging through NV magnetometry[97]. A still outstanding challenge is to extend such studies to single-crystalline, skyrmion-hosting materials[116], in which pristine skyrmion behaviour, including collective modes in skyrmion lattices[117], and possibly even quantum dynamics of skyrmions[118], could be examined in the future.

Superconducting order

By locally probing the magnetic response of a superconductor, it is possible to image superconducting order and various parameters of the superconducting state. The magnetic (London) penetration depth λ_L determines the length scale over which magnetic field lines can enter a superconductor before Meissner screening becomes effective. Quantitative determinations of λ_L, together with its temperature dependence and spatial anisotropy, provide valuable insights into superfluid density and pairing mechanism of a superconductor[119]. Specifically, λ_L determines the superfluid density — the number of electrons that superconduct[120].

NV magnetometry has been employed to directly measure the penetration depth, particularly in high-temperature superconductors[19,21,121,122]. This has, for instance, been achieved by imaging vortices in type II superconductors, in which quantitative analysis of vortex stray fields yields the London penetration depth, or the Pearl length (for cases in which the film thickness is small compared with λ_L)[19]. Alternatively, λ_L has also been determined by direct measurements of Meissner screening in superconductor microstructures[121] and a superconducting strip on a thin-film magnetic insulator[123] or using wide-field NV magnetometry[124]. This latter approach is notably applicable to type I superconductors as well.

Two particularly noteworthy, recent examples demonstrated the new opportunities that NV magnetometry brings to the field of superconductivity. In the first study[123], an NV probe was used to scan a hybrid system consisting of a strip of a superconductor placed on a ferromagnetic substrate, in which the diamagnetic response of the superconductor locally altered the propagation of spin waves in the ferromagnet. This not only opened new avenues in magnonics[125] but also demonstrated a novel method to determine the temperature dependence of λ_L. In the second example[126], NV magnetometry was employed for current imaging of supercurrent flow across Josephson junctions, which form central building blocks for high-precision magnetometers and other quantum devices. This study uncovered competing ground states in the Josephson junction and identified a new mechanism for the Josephson diode effect, both of which highlight the novel insights NV magnetometry offers into the study of superconductivity and superconducting devices.

Such studies of superconductor properties by quantitative NV magnetometry have thus far been applied to reasonably well-understood superconductors (such as yttrium barium copper oxide), deep in the type II limit of superconductivity. Future worthwhile extensions include the study of vortices in superconductors at the crossover between type I and type II superconductivity, where vortex stray fields are still poorly understood and can only be described by approximative or numerical models[127–129]. Such experiments might offer the interesting perspective of simultaneously determining λ_L and the superconductor coherence length ξ by direct magnetic imaging.

NV centres incorporated into a DAC allow for local magnetic imaging of materials under high, ~100 GPa, pressures[39–42]. High pressure presents an important knob for tuning microscopic interactions and has led to the discovery of novel high temperature superconductors[130]. Recent work[43] used an NV-infused DAC to image the spatial structure of superconducting regions in a hydride superconductor at the micrometre scale, revealing substantial inhomogeneities and informing the materials synthesis of superhydrides (Fig. 2b). Although it is non-trivial to maintain magnetic sensitivity of NV centres at these high pressures, there are ongoing efforts to extend the pressure range higher[42,43], a frontier for spatially resolved magnetic imaging.

In all such studies, care must be taken to minimize perturbations of the superconducting state by NV microwave and laser excitation, to maintain a non-invasive measurement. Although each sample and material will show a different response to such perturbations, a careful investigation of laser heating during NV magnetometry experiments on thin-film yttrium barium copper oxide showed that appreciable heating only became apparent at laser powers that exceed the typical working conditions of scanning NV magnetometry by a factor of 10 (ref. 19). More fragile superconductors will likely require more delicate sensing protocols, such as pulsed sensing schemes[131].

Current imaging

Electrical currents produce magnetic fields according to the Biot–Savart law that can be detected and imaged via NV centre magnetometry. Spatial maps of current patterns in a device can distinguish different scattering mechanisms in a material, providing much more information than a standard transport measurement that yields just one number — the spatially averaged conductivity. For instance, the path that electrons take in a device depends on the relative strengths of momentum-conserving scattering (electron–electron scattering) and momentum-relaxing scattering (electron–phonon or impurity scattering).

Recently, NV magnetometry has been applied to quantitatively probe different transport regimes in a few electronic materials[17,18,63], in particular looking for spatial signatures of current flow in the rare electron hydrodynamic regime, in which electron–electron scattering dominates and electrons move akin to fluids. Several device geometries that produce distinctive flow patterns in the hydrodynamic, ballistic and Ohmic regimes have been proposed and experiments have begun to reveal signatures of hydrodynamics. However, the critical influence of boundary conditions[132], the possibility of ballistic vortices masquerading as viscous vortices and small angle scattering leading to para-hydrodynamics[133] demand a more complete understanding.

Nevertheless, direct spatial mapping of the current flow provides much more direct evidence of hydrodynamic behaviour than transport measurements and, importantly, provides a way to quantitatively probe the importance of electron–electron interactions (Fig. 2c). Hence, NV magnetometry measurements can be used for

understanding other open questions in condensed matter, such as the role of electron–electron interactions in the superconductivity of graphene[134]. Spatially resolved current imaging can also reveal local current anomalies or irregularities (such as those stemming from impurities), whose presence can greatly affect the interpretation of a standard transport measurement, leading to incorrect conclusions.

Dynamics

In equilibrium, the response of a material is related to its intrinsic thermal or quantum fluctuations (or the noise it generates) by the fluctuation-dissipation theorem[135]: for example, the conductivity at frequency ω is related to the Fourier transform of the current autocorrelation function, which can be measured using NV magnetometry. In systems that are driven out of equilibrium, fluctuations and response contain distinct information about the state of the system: to characterize the steady state, one needs separate access to both quantities. For example, current noise in non-equilibrium states is sensitive to properties such as the charge of individual carriers[136], to which equilibrium transport does not give access. Most solid-state experimental setups used to study noise[137,138] are restricted to measuring current noise in essentially 1D geometries. NV centres can overcome this restriction and sense local current or magnetic-field fluctuations in 2D systems. They can therefore be used to explore questions about non-equilibrium noise that would not previously have been experimentally accessible. In addition, even in equilibrium, NV centres are unique in having the ability to probe local wavevector-dependent current noise.

Noise from a nearby material can affect the NV centre either by depolarizing it and decreasing its T_1 time or by dephasing it and affecting its T_2 time. Accordingly, an NV centre can be used as a noise sensor in one of the two basic modes, relaxometry (T_1) and Ramsey (T_2) spectroscopy. In what follows, we outline how an NV centre couples to noise in the underlying sample, then review these two basic spectroscopic protocols, as well as recent extensions that involve measuring correlations among multiple NV centres.

What an NV centre senses

The response of an NV centre to a sample with Hamiltonian H_{sample} can be complicated in the general case; for instance, the magnetic field $\hat{\mathbf{B}}$ that couples to the NV centre is (in general) operator-valued, so $[\hat{\mathbf{B}}, \hat{H}_{\text{sample}}] \neq 0$, resulting in an intractable Hamiltonian. To gain a better understanding of the properties of the system from the NV centre response, we will make various approximations to arrive at a simpler effective Hamiltonian.

The first, most natural simplification is to note that the field at the NV centre is determined by the properties of a relatively large patch (of diameter ≥10 nm) of the sample. In most condensed matter contexts, there are many active degrees of freedom in a patch of this size. Although each degree of freedom is quantum, the average of the current or magnetic field over a patch of this size can be treated as a classical stochastic variable. This allows us to describe the NV as a qubit driven by a time-dependent classical field $\mathbf{B}$, so

$$\hat{H}_{\text{NV}} = D_{\text{zfs}}\hat{S}_z^2 - \gamma_e \mathbf{B}(t)\cdot\hat{\mathbf{S}}, \quad (1)$$

in which S_i are the spin-1 operators. It suffices to relate the statistics of $\mathbf{B}(t)$ to those of the dynamical fluctuations in the underlying sample and to characterize the dynamics of the qubit for $\mathbf{B}(t)$ drawn from such an ensemble.

A sample can generate a magnetic field at the NV centre either because it has magnetic fluctuations or because it has fluctuating currents $\mathbf{J}(\mathbf{x}, t)$ that induce a magnetic field at the NV centre in a way that depends on the distance $\mathbf{x}$ to the NV centre. In either case, there is a linear kernel relating the magnetic field at the NV centre to the relevant fluctuating field in the sample. In general, this kernel can be non-local in time, and this non-locality can have substantial effects in 3D metals, in which current fluctuations have to travel through the metal to reach the NV. However, the situation is simpler in two dimensions, and one can generally make a quasistatic approximation so that the field at the NV centre is linearly related to the current (or, with the obvious modifications, the magnetization) in the sample near the NV centre, by an expression of the form $B_i(t) = \sum_{j=1}^{3}\int \mathrm{d}^3\mathbf{x} K_{ij}(\mathbf{x}, t)J_j(\mathbf{x}, t)$, in which i and j are Cartesian coordinates. For quasistatic currents, the kernel K_{ij} is given by the Biot–Savart law (equation (7)), but more generally it will be some convolution of the current (or magnetization) fluctuations in the sample over a length scale d.

T_1 spectroscopy

One of the earliest applications of NV centres to studying transport involved T_1 noise spectroscopy of Johnson noise from silver films[37]. One can relate the T_1 time of the NV to the autocorrelation tensor of the current in the sample, which in turn can be related (via the fluctuation-dissipation theorem) to the momentum-dependent conductivity (Box 2). In the interests of brevity, we have sketched the derivation of Box 2 in the simplest case; however, the strategy outlined there can be adapted to any form of current noise under the quasi-static approximation (equation (7)). By varying the polarizing field and the height of the NV centre from the sample (for example, by using an ensemble of NV centres at different heights), one can tune q and ω. In principle, by varying the orientation of the sample with respect to the quantization axis, one can also extract angle-dependent information about the correlations of current noise.

For diffusive transport in the local approximation, the same formalism may be applied to directly measure conductivity, enabling nanoscale conductivity imaging of inhomogeneous materials[25] (Fig. 3a). Beyond linear response theory, recent work used spatially resolved T_1 relaxometry in conjunction with global transport to study anomalous noise in graphene transport[27]. This noise was attributed to an electron–phonon Cerenkov instability, as the rate of stimulated emission of phonons exceeded their absorption rate in pristine graphene (Fig. 3b). The ability to spatially resolve the noise source using NV centres, revealing that the noise amplification followed charge carriers rather than current, was a critical tool in diagnosing the effect.

Relaxometry has also been applied to the study of magnetic excitations, for example, to study thermally excited magnons in permalloy and yttrium iron garnet[38,139], in which the NV relaxation rate is accurately described by models accounting for the number and spectral density of magnons, as well as the interplay between the magnon $\mathbf{k}$-vector and NV-sample distance. Beyond thermal magnons, related studies explored ferromagnetic resonance in driven magnetic systems, describing the mechanism behind broadband NV spin relaxation and demonstrating coherent interactions between NV centres and spin waves[140–145]. More recently, NV centres have enabled wavenumber-resolved magnon measurements[23,24,146] (Fig. 3c), the development of a magnon scattering platform based on real-space imaging of spin waves scattered off a target[26], and the detection of spin waves generated by nonlinear multimagnon scattering[147]. NV centre relaxometry also enables local measurements of magnetic phase transitions[148], as the increased spin

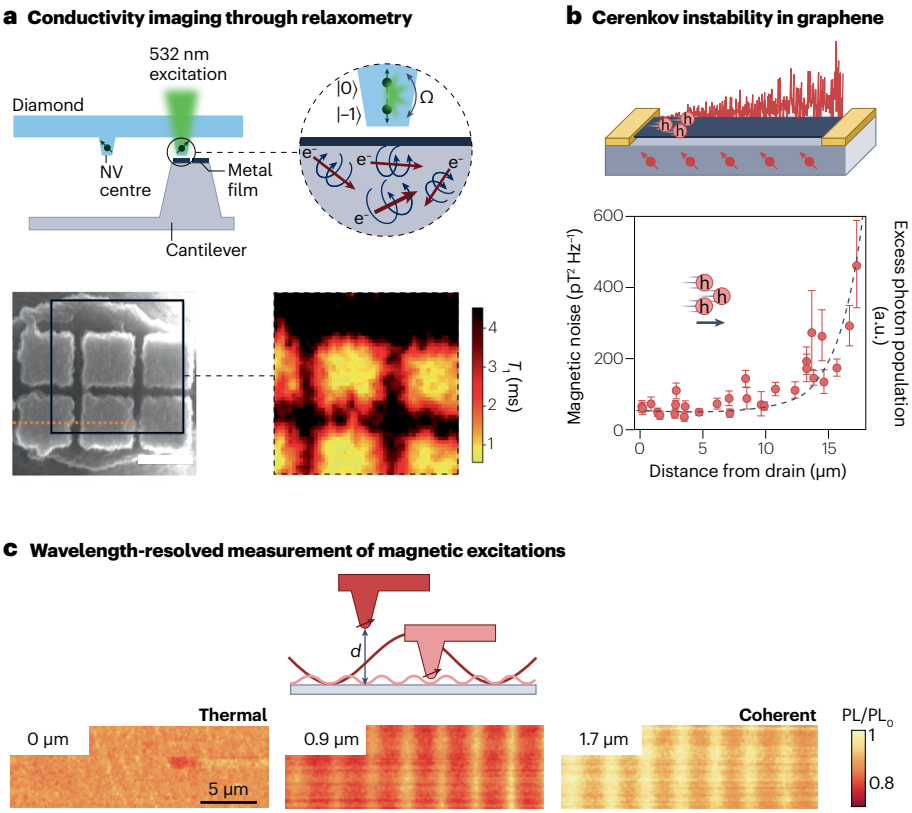

Fig. 3 | Sensing dynamics through relaxometry. **a**, Nanoscale conductivity imaging, using nitrogen vacancy (NV) centre relaxometry induced by thermal electron motion in the metal. Imaging of an Al nanopattern resolves features down to 5 nm (bottom), where the scale bars are 400 nm. **b**, Electronic noise in graphene exhibiting amplification along the transport direction, detected using proximal NV centres. Spatially resolved noise magnetometry was used to diagnose the anomalous noise as arising from an electron–phonon Cerenkov instability at high current. **c**, Wavelength-resolved imaging of magnetic excitations in yttrium iron garnet using the distance dependence of the stray field filter function[24]. Spin waves are excited using a microwave stripline, then self-interact through magnon–magnon interactions creating local magnetic noise. Near the sample, short-wavelength incoherent thermal magnons dominate the NV centre relaxation, whereas further from the stripline, long-wavelength coherent magnons at the NV centre transition frequency drive NV centre Rabi oscillations. Panel **a** is adapted with permission from ref. 25. The bottom part of panel **b** is reprinted with permission from ref. 27. Panel **c** is adapted with permission from ref. 24. a.u., arbitrary unit.

susceptibility near the critical point causes a peak in local magnetic noise (Box 2). This technique has recently been used to spatially map the distinct phase transitions of ferromagnetic and antiferromagnetic phases that exist side-by-side in the moire superlattice formed by twisted van der Waals CrI_3 (ref. 149), a demonstration of the combined benefits of non-invasive nanoscale imaging and high-sensitivity noise magnetometry for studying magnetic systems[150].

Theoretical studies suggest that T_1 spectroscopy can be used to probe other phenomena in correlated electron systems, for instance, to analyse Bogoliubov quasiparticles in low-dimensional superconductors[151,152]. Such experiments can distinguish gapless and fully gapped quasiparticles by measuring noise from current and spin fluctuations as a function of temperature, enabling identification of different symmetries of the order parameter (*s*-wave versus *d*-wave)[152]. Another potential application of this technique is to probe 1D systems, such as domain walls in antiferromagnetically ordered materials[153], or edge states in topological systems. These studies can elucidate the mechanism of electron scattering, which is still poorly understood[154]. Finally, a promising application of NV relaxometry is to probe spin liquid states, in which magnetic noise should provide signatures of different types of spinon dynamics[155,156].

T_2 spectroscopy

Although T_1 spectroscopy has the advantage of probing relatively high frequencies (in the gigahertz range), it has limited bandwidth and also provides relatively coarse information about the structure of the noise. For probing a wider range of low frequencies and for addressing more detailed questions such as the character, spectrum and non-Gaussianity of the noise, T_2 spectroscopy offers a more versatile approach. The basic idea behind T_2 spectroscopy is to initialize the NV centre on the equator of the Bloch sphere and have it precess in the fluctuating field from the sample. Unlike T_1 spectroscopy, this approach senses the field along the quantization axis; for T_2 spectroscopy to be useful, the noise at the transition frequency of the NV should be negligible to avoid depolarization during the T_2 measurement.

Suppose that the NV centre is initialized in the spin state $|+\rangle \equiv \frac{1}{\sqrt{2}}(|0\rangle + |1\rangle)$. We choose the quantization axis of the NV to be the *z*-axis of its Bloch sphere and define $B_\parallel$ to be the component of the local magnetic field along the quantization axis (the choice of basis on the Bloch sphere is in general distinct from the real-space coordinate system). After free evolution for a time t, the NV centre is in a state $|\psi(t)\rangle = \frac{1}{\sqrt{2}}(|0\rangle + e^{-i\phi_t}|1\rangle)$, in which $\phi_t = -\gamma_e \int_0^t \mathrm{d}t'\, B_\parallel(t')$. One can interrupt this evolution with various pulse sequences borrowed from the NMR literature[35]; in this case, the expression for the accumulated phase generalizes to[157]:

$$\phi_t = -\gamma_e \int_0^t \mathrm{d}t'\, s(t') B_\parallel(t'), \qquad (2)$$

in which $s(t')$ is the filter function for a particular pulse sequence. For example, in a standard spin-echo sequence, $s(t') = \mathrm{sign}(t/2 - t')$. At the end of the sequence, one measures the NV centre in the *x* and *y* bases; the results can be combined to reconstruct the expectation value $\langle e^{i\phi_t} \rangle$. If the noise has zero mean, and the filter function satisfies $\int_0^t \mathrm{d}t' s(t') = 0$, one can use the cumulant expansion to write $\langle e^{i\phi_t} \rangle = \exp(-\langle \phi_t^2 \rangle/2 + \ldots)$, in which … contains non-Gaussian corrections. This relates the dephasing rate of the NV centre to the correlation function:

$$C_\phi(t) = \gamma_e^2 \int_0^t \int_0^t dt' dt'' s(t') s(t'') \langle B_\parallel(t') B_\parallel(t'') \rangle. \quad (3)$$

Finally, the magnetic field at the NV centre can be related to the current in the sample through equation (7). The filter function $s(t)$ controls the range of frequencies that contribute to decoherence: for example, if $s(t)$ is a series of π pulses spaced by τ, noise below π/τ will be echoed out and will not contribute to decoherence. Although pulse-defined filter function bandwidths are limited by the NV centre driving rates (typically less than 100 MHz), new antenna designs and pulse protocols have extended the range for particular experiments[158–160].

Unlike T_1 spectroscopy, which is primarily sensitive to the power spectrum of the noise, T_2 spectroscopy allows one to detect higher-order correlations in the noise. An explicit non-Gaussian example, for a qubit driven by telegraph noise, was worked out in ref. 161. Exploring such non-Gaussian effects in many-body systems (such as near-phase transitions) and their signatures in NV magnetometry remains an important task for future research.

Most applications of T_2 spectroscopy to date have been in the Gaussian approximation and make use of a periodic pulse sequence to approximately select a single frequency at a time (assuming that the pulse sequence filter function is non-zero only at a single frequency f, see equation (6)). This approach has found use in studying environmental noise spectra to diagnose NV centre dephasing sources, especially near surfaces, where dimensional analysis allows the shape of the coherence decay to report on the nature of the noise bath[29,30,61]. Dynamical decoupling can also be used to selectively couple NV centres to nuclear spins by matching the pulse rate to a multiple of the nuclear Larmor frequency; although most examples of nuclear spin sensing have targeted biological applications[87,162], an example in condensed matter includes the measurement of nuclear quadrupole resonance in hexagonal boron nitride[163]. Other recent applications of T_2 measurements of electronic systems include the observation of increased NV centre coherence times in proximity to a superconductor[22] and local superconductor imaging through transverse spin relaxometry leveraging this effect[164].

Beyond the Gaussian approximation, the shape of the coherence decay can reveal dynamical transitions that provide information about the correlation time of the noise[29,30], which may be deployed to study dynamics in condensed matter systems (Fig. 4a). Such noise spectroscopy can provide insights into phase transitions by measuring the qubit relaxation rate as the system is tuned near its critical point[165]. The scaling of the NV centre dephasing $\langle \phi_t^2 \rangle$ with measurement time and, in particular, its dependence on temperature T relative to the critical temperature T_c and on the NV-sample distance d relative to the correlation length ξ can report on the critical exponents of the transition as the system is tuned near criticality (Fig. 4b). In a recent study of magnetic fluctuations in trilayer CrSBr (ref. 166), the critical exponent of the fluctuation correlation length was extracted from the NV centre T_2 decay rate using this method and was shown to differ from the Ising

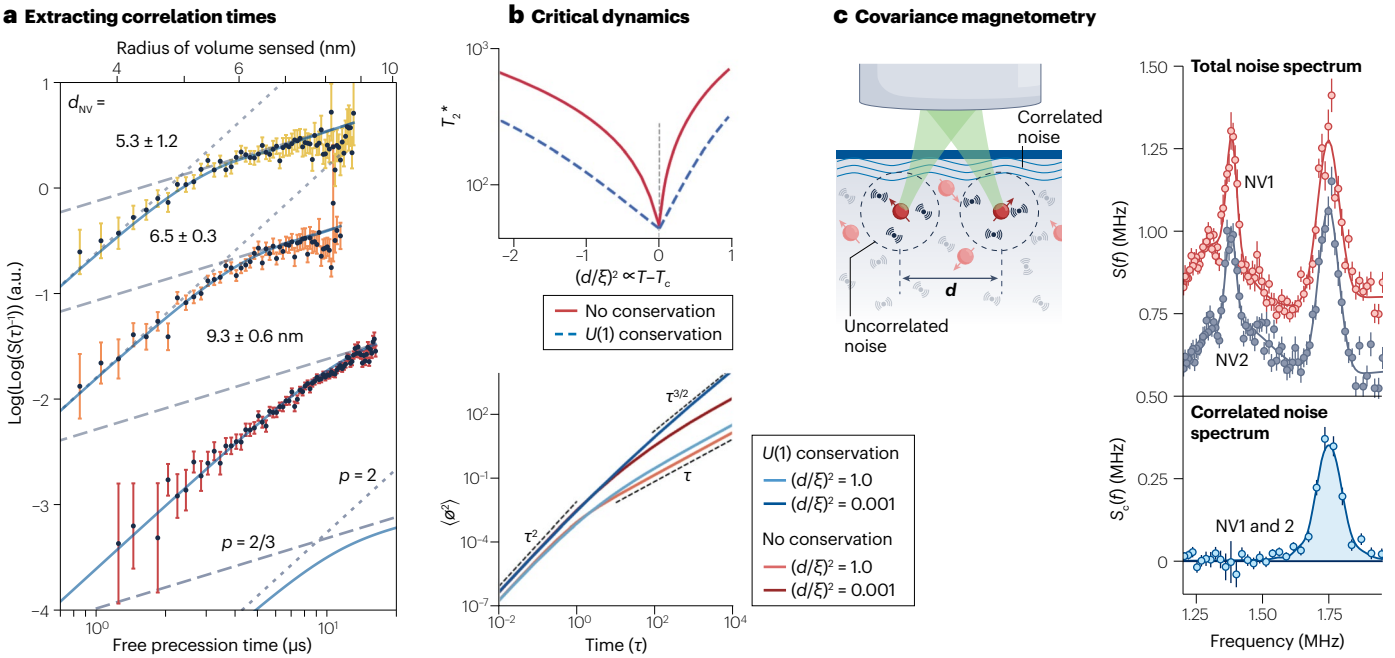

Fig. 4 | Ramsey-based noise spectroscopy. a, The exponential stretching factor p, derived from the nitrogen vacancy (NV) centre coherence decay $C(t) = \exp[-(t/T_2)^p]$ through the slope of the straight lines, undergoes a transition at a depth-dependent critical time determined by the correlation time of the noise, from $p = 2$ (Gaussian) decay to $p = 2/3$, consistent with a reconfiguring 2D noise bath. **b**, Near a phase transition, the dephasing time T_2^* (upper panel) and decoherence dynamics similar to those shown in panel **a** (lower panel) can characterize the transition (for example, diagnose the critical temperature T_c and the presence of order parameter conservation) through their dependence on the system temperature relative to T_c and on the NV-sample distance d relative to the correlation length ξ (ref. 165). **c**, The schematic shows that two NV centres experience fluctuating magnetic fields that are correlated (as from correlated excitations in a target condensed matter system) or uncorrelated (as from local fluctuating nuclear spins) between the locations of the two NV centres. Although two NV centres 1 and 2 may be used as individual spectrometers of their local noise spectra (right, top), covariance spectroscopy reveals which noise sources are correlated and which are uncorrelated between the two NV centres (right, bottom). Panel **a** is adapted with permission from ref. 29. Panel **b** is adapted with permission from ref. 165. The right part of panel **c** is adapted with permission from ref. 28.

prediction. The ability to detect this discrepancy, attributed to the influence of long-range dipolar interactions, shows the usefulness of coherent noise magnetometry for measuring magnetic dynamics in atomically thin systems.

Covariance sensing

The spectroscopic methods described earlier are spatially resolved in the sense that an NV centre at distance d from the sample will sense noise that is averaged over a length scale d. However, there are both technical and fundamental limitations to how much spatial information one can extract. At the technical level, moving the NV centre far from the sample makes it couple more weakly, limiting the scope for sensing long-range correlations. More fundamentally, extracting two-point temporal correlation functions from equations (2) is only possible if one assumes the noise to be stationary in time; this assumption fails in many non-equilibrium settings. A recently developed technique circumvents these limitations by using multiple NV centres to directly measure correlation functions[28] (Fig. 4c).

The simplest version of the covariance sensing protocol proceeds as follows. Two NV centres are initialized, at positions $\mathbf{x}_1$ and $\mathbf{x}_2$, and times t_1 and t_2, along the equator of the Bloch sphere. They precess in a spatiotemporally correlated magnetic field $\mathbf{B}(\mathbf{x}, t)$ from the underlying sample. Finally, the phase is mapped to population and both NV centres are measured along the z-axis. The classical correlation between these measurement outcomes is related to the correlation between the phase picked up by the two NV centres, which can be reduced (as before) to the noise correlations in the sample. In practice, because of the limited detection efficiency for each measurement, the number of measurements required for a precise estimate of the correlation function is quite large, although it has been mitigated using higher fidelity readout schemes such as spin-to-charge conversion[71]. In a proof-of-principle experiment, it was shown that a noise sensitivity of ~100 $nT^2Hz^{-1/2}$ could be achieved using this approach[28], improvable with readout methods optimally tailored to detect multiple NV centres. Related recent experiments have used resonant optical readout of NV centres at low temperature to detect correlated electric field dynamics induced by local trapped charges in the diamond[167,168].

Non-local covariance measurements may reveal details about the intrinsic length scale and timescale of dynamics detected through fluctuating electromagnetic fields, which are characterized by non-local two-point field correlators[151,152], complementing tools such as neutron scattering which averages over the bulk of the material, and scanning probes which are fundamentally local. The development of high-sensitivity covariance sensing across many NV centres simultaneously, as well as scanning experiments enabling high-resolution distance scanning, could enable progress studying rich noise dynamics found in hydrodynamic electron flow[48,49], spin liquids[169] and other phenomena in which structure factors would otherwise be obscured by locally uniform noise.

Outlook

NV magnetometry can shed light on the microscopic origin of magnetically ordered condensed matter systems, which exhibit only weak, uncompensated moments. A prime example is antiferromagnetic order, which is typically considered unsuitable for direct magnetic imaging. There, NV magnetometry has already found applications, for example, in magnetoelectrics[14,102,170,171], in which uncompensated surface moments collinear with the bulk Néel vector of antiferromagnets intrinsically occur[172] and are measurable by NV magnetometry. A question of high relevance is how generally applicable NV magnetometry is to the study of antiferromagnetism. Indeed, the occurrence of weak, uncompensated moments appears ubiquitous in antiferromagnets. Mechanisms such as spin canting (owing to chiral spin–spin interactions[173]) or spatially inhomogeneous Néel vector spin textures[174] have been predicted to lead to such moments and thereby to non-zero stray magnetic fields that may be detectable by NV magnetometry. Such mechanism would enable generic approaches, such as nanoscale domain imaging in antiferromagnets using static magnetic imaging, an exciting avenue that remains to be explored in the future.

Further avenues for study using DC NV magnetometry in condensed matter physics include the nature and existence of time-reversal symmetry breaking, for example, in quasi-2D Kagome materials[175] or in unconventional superconductors such as Sr_2RuO_4 (ref. 176). Observations of time-reversal symmetry breaking in this presumably non-magnetic compound could be explained by long-theorized, yet elusive, flux phases[177]; local, quantitative and sensitive experimental probes are necessary to validate the theories. For instance, the recent experimental demonstrations of orbital magnetism in Moiré systems[178] imply many potential applications, but very little is known about the underlying origin of this unusual magnetism and its relations to topology and electron correlations.

Beyond imaging magnetic structure, two natural settings in which NV centres can provide fundamentally new information about condensed matter systems are systems that are strongly spatially inhomogeneous on nanometre length scales and systems driven out of equilibrium. The former class includes a wide variety of strongly correlated 2D systems, from disordered superconducting films[179] to cuprates[180] and Moiré materials[181], as well as phenomena such as 2D metal-to-insulator transitions[182–185]. In all of these systems, there is substantial evidence for spatial inhomogeneity, mostly from STM experiments. NV centres offer a complementary probe: instead of measuring the local density of states (as STM does), it measures the local magnetic field at the surface, allowing one to probe finite-frequency fluctuations with very high spatial resolution. The insights from NV sensing have the potential to shed light on many longstanding puzzles involving the role of spatial inhomogeneity or rare-region effects on quantum phases and phase transitions in two dimensions[186,187].

For systems driven out of equilibrium, NV sensing (especially T_2 sensing, covariance magnetometry and related approaches) can shed new light on many-body physics that involves phase transitions and collective phenomena. Non-equilibrium driving, either transiently (for example, through a sudden current pulse) or in the presence of a steady-state current drive, is known to change the critical properties at quantum phase transitions[188,189] and also to give rise to phenomena such as light-induced superconductivity[190]. In these non-equilibrium states, current noise inherently carries information that is distinct from transport; in certain models, one can explicitly show that non-equilibrium noise allows one to distinguish between physical mechanisms that have very similar transport signatures. By shedding light on these mechanisms, nanoscale noise sensing has the potential to discriminate between the many proposed physical mechanisms for unconventional collective behaviour in correlated systems. Improving NV centre coherence times and spatial resolution towards their respective fundamental limits of milliseconds and nanometres, especially for shallow NV centres, will be enabling for nanoscale noise spectroscopy as well as for high-resolution imaging of the weak stray fields described earlier.

Finally, beyond magnetometry, NV centres are useful for the detection of electric fields[191], temperature[192] and strain[193], which has already proven useful, for instance, in measurements using DACs[39,40] as described earlier. Looking forward, this multifaceted utility of NV centres in diamond can provide unique advantages in sensing condensed matter systems, for instance, in correlating heat transport and electronic transport for studying deviations from the Wiedemann–Franz law[194] in low-dimensional systems[195].

Published online: 11 November 2024

References

1. Vojta, T. Quantum Griffiths effects and smeared phase transitions in metals: theory and experiment. *J. Low Temp. Phys.* **161**, 299–323 (2010).
2. Jamei, R., Kivelson, S. & Spivak, B. Universal aspects of Coulomb-frustrated phase separation. *Phys. Rev. Lett.* **94**, 056805 (2005).
3. Huang, E. W. et al. Numerical evidence of fluctuating stripes in the normal state of high-T_c cuprate superconductors. *Science* **358**, 1161–1164 (2017).
4. Yazdani, A., Da Silva Neto, E. H. & Aynajian, P. Spectroscopic imaging of strongly correlated electronic states. *Annu. Rev. Condens. Matter Phys.* **7**, 11–33 (2016).
5. Yin, J.-X., Pan, S. H. & Zahid Hasan, M. Probing topological quantum matter with scanning tunnelling microscopy. *Nat. Rev. Phys.* **3**, 249–263 (2021).
6. Jäck, B., Xie, Y. & Yazdani, A. Detecting and distinguishing Majorana zero modes with the scanning tunnelling microscope. *Nat. Rev. Phys.* **3**, 541–554 (2021).
7. Barber, M. E., Ma, E. Y. & Shen, Z.-X. Microwave impedance microscopy and its application to quantum materials. *Nat. Rev. Phys.* **4**, 61–74 (2021).
8. Persky, E., Sochnikov, I. & Kalisky, B. Studying quantum materials with scanning SQUID microscopy. *Annu. Rev. Condens. Matter Phys.* **13**, 385–405 (2022).
9. Hartmann, U. Magnetic force microscopy. *Annu. Rev. Mater. Sci.* **29**, 53–87 (1999).
10. Balasubramanian, G. et al. Nanoscale imaging magnetometry with diamond spins under ambient conditions. *Nature* **455**, 648–651 (2008).
11. Tetienne, J. P. et al. The nature of domain walls in ultrathin ferromagnets revealed by scanning nanomagnetometry. *Nat. Commun.* **6**, 6733 (2014).
12. Casola, F., van der Sar, T. & Yacoby, A. Probing condensed matter physics with magnetometry based on nitrogen-vacancy centres in diamond. *Nat. Rev. Mater.* **3**, 17088 (2018).
13. Rondin, L. et al. Magnetometry with nitrogen-vacancy defects in diamond. *Rep. Progr. Phys.* **77**, 56503 (2014).
14. Appel, P. et al. Nanomagnetism of magnetoelectric granular thin-film antiferromagnets. *Nano Letters* **19**, 1682 (2019).
15. Finco, A. et al. Imaging non-collinear antiferromagnetic textures via single spin relaxometry. *Nat. Commun.* **12**, 767 (2021).
16. Haykal, A. et al. Antiferromagnetic textures in $BiFeO_3$ controlled by strain and electric field. *Nat. Commun.* **11**, 1704 (2020).
17. Vool, U. et al. Imaging phonon-mediated hydrodynamic flow in WTe_2. *Nat. Phys.* **17**, 1216–1220 (2021).
18. Jenkins, A. et al. Imaging the breakdown of Ohmic transport in graphene. *Phys. Rev. Lett.* **129**, 087701 (2022).
19. Thiel, L. et al. Quantitative nanoscale vortex imaging using a cryogenic quantum magnetometer. *Nat. Nanotechnol.* **11**, 677–681 (2016).
20. Pelliccione, M. et al. Scanned probe imaging of nanoscale magnetism at cryogenic temperatures with a single-spin quantum sensor. *Nat. Nanotechnol.* **11**, 700–705 (2016).
21. Schlussel, Y. et al. Wide-field imaging of superconductor vortices with electron spins in diamond. *Phys. Rev. Appl.* **10**, 034032 (2018).
22. Monge, R. et al. Spin dynamics of a solid-state qubit in proximity to a superconductor. *Nano Lett.* **23**, 422–428 (2023).
23. Lee-Wong, E. et al. Nanoscale detection of magnon excitations with variable wavevectors through a quantum spin sensor. *Nano Lett.* **20**, 3284–3290 (2020).
24. Simon, B. G. et al. Filtering and imaging of frequency-degenerate spin waves using nanopositioning of a single-spin sensor. *Nano Lett.* **22**, 9198–9204 (2022).
25. Ariyaratne, A., Bluvstein, D., Myers, B. A. & Jayich, A. C. B. Nanoscale electrical conductivity imaging using a nitrogen-vacancy center in diamond. *Nat. Commun.* **9**, 2406 (2018).
26. Zhou, T. X. et al. A magnon scattering platform. *Proc. Natl Acad. Sci. USA* **118**, e2019473118 (2021).
27. Andersen, T. I. et al. Electron–phonon instability in graphene revealed by global and local noise probes. *Science* **364**, 154–157 (2019).
28. Rovny, J. et al. Nanoscale covariance magnetometry with diamond quantum sensors. *Science* **378**, 1301–1305 (2022).
29. Dwyer, B. L. et al. Probing spin dynamics on diamond surfaces using a single quantum sensor. *PRX Quant.* **3**, 040328 (2022).
30. Davis, E. J. et al. Probing many-body dynamics in a two-dimensional dipolar spin ensemble. *Nat. Phys.* **19**, 836–844 (2023).
31. Joos, M., Bluvstein, D., Lyu, Y., Weld, D. & Bleszynski Jayich, A. Protecting qubit coherence by spectrally engineered driving of the spin environment. *npj Quant. Inform.* **8**, 47 (2022).
32. Maze, J. R. et al. Nanoscale magnetic sensing with an individual electronic spin in diamond. *Nature* **455**, 644–647 (2008).
33. Abobeih, M. H. et al. Atomic-scale imaging of a 27-nuclear-spin cluster using a quantum sensor. *Nature* **576**, 411–415 (2019).
34. Marchiori, E. et al. Nanoscale magnetic field imaging for 2D materials. *Nat. Rev. Phys.* **4**, 49–60 (2021).
35. Vandersypen, L. M. K. & Chuang, I. L. NMR techniques for quantum control and computation. *Rev. Mod. Phys.* **76**, 1037–1069 (2005).
36. Balasubramanian, G. et al. Ultralong spin coherence time in isotopically engineered diamond. *Nat. Mater.* **8**, 383–387 (2009).
37. Kolkowitz, S. et al. Probing Johnson noise and ballistic transport in normal metals with a single-spin qubit. *Science* **347**, 1129–1132 (2015).
38. Du, C. et al. Control and local measurement of the spin chemical potential in a magnetic insulator. *Science* **357**, 195–198 (2017).
39. Hsieh, S. et al. Imaging stress and magnetism at high pressures using a nanoscale quantum sensor. *Science* **366**, 1349–1354 (2019).
40. Lesik, M. et al. Magnetic measurements on micrometer-sized samples under high pressure using designed NV centers. *Science* **366**, 1359–1362 (2019).
41. Yip, K. Y. et al. Measuring magnetic field texture in correlated electron systems under extreme conditions. *Science* **366**, 1355–1359 (2019).
42. Hilberer, A. et al. Enabling quantum sensing under extreme pressure: nitrogen-vacancy magnetometry up to 130 GPa. *Phys. Rev. B* **107**, L220102 (2023).
43. Bhattacharyya, P. et al. Imaging the Meissner effect in hydride superconductors using quantum sensors. *Nature* **627**, 73–79 (2024).
44. Boothroyd, A. T. Basic concepts. in *Principles of Neutron Scattering from Condensed Matter* 1st edn, 1–30 https://academic.oup.com/book/43701/chapter/367125595 (Oxford Univ. Press, 2020).
45. Ament, L. J. P., Van Veenendaal, M., Devereaux, T. P., Hill, J. P. & Van Den Brink, J. Resonant inelastic X-ray scattering studies of elementary excitations. *Rev. Mod. Phys.* **83**, 705–767 (2011).
46. Vig, S. et al. Measurement of the dynamic charge response of materials using low-energy, momentum-resolved electron energy-loss spectroscopy (M-EELS). *SciPost Phys.* **3**, 026 (2017).
47. Dolgirev, P. E. et al. Local noise spectroscopy of Wigner crystals in two-dimensional materials. *Phys. Rev. Lett.* **132**, 246504 (2024).
48. Agarwal, K. et al. Magnetic noise spectroscopy as a probe of local electronic correlations in two-dimensional systems. *Phys. Rev. B* **95**, 155107 (2017).
49. Lucas, A. & Fong, K. C. Hydrodynamics of electrons in graphene. *J. Phys. Condens. Matter* **30**, 053001 (2018).
50. Christensen, D. V. et al. 2024 Roadmap on magnetic microscopy techniques and their applications in materials science. *J. Phys. Mater.* **7**, 032501 (2024).
51. Abobeih, M. H. et al. One-second coherence for a single electron spin coupled to a multi-qubit nuclear-spin environment. *Nat. Commun.* **9**, 2552 (2018).
52. Childress, L. & Hanson, R. Diamond NV centers for quantum computing and quantum networks. *MRS Bull.* **38**, 134–138 (2013).
53. Toyli, D. M. et al. Measurement and control of single nitrogen-vacancy center spins above 600 K. *Phys. Rev. X* **2**, 031001 (2012).
54. Liu, G.-Q., Feng, X., Wang, N., Li, Q. & Liu, R.-B. Coherent quantum control of nitrogen-vacancy center spins near 1000 kelvin. *Nat. Commun.* **10**, 1344 (2019).
55. Fortman, B. et al. Electron–electron double resonance detected NMR spectroscopy using ensemble NV centers at 230 GHz and 8.3 T. *J. Appl. Phys.* **130**, 083901 (2021).
56. Hart, C. A. et al. NV-diamond magnetic microscopy using a double quantum 4-Ramsey protocol. *Phys. Rev. Appl.* **15**, 044020 (2021).
57. Wan, N. H. et al. Efficient extraction of light from a nitrogen-vacancy center in a diamond parabolic reflector. *Nano Lett.* **18**, 2787–2793 (2018).
58. Hedrich, N., Rohner, D., Batzer, M., Maletinsky, P. & Shields, B. J. Parabolic diamond scanning probes for single-spin magnetic field imaging. *Phys. Rev. Appl.* **14**, 064007 (2020).
59. Aharonovich, I. et al. Homoepitaxial growth of single crystal diamond membranes for quantum information processing. *Adv. Mater.* https://onlinelibrary.wiley.com/doi/10.1002/adma.201103932 (2012).
60. Guo, X. et al. Tunable and transferable diamond membranes for integrated quantum technologies. *Nano Lett.* **21**, 10392–10399 (2021).
61. Sangtawesin, S. et al. Origins of diamond surface noise probed by correlating single-spin measurements with surface spectroscopy. *Phys. Rev. X* **9**, 031052 (2019).
62. Choi, J. et al. Robust dynamic Hamiltonian engineering of many-body spin systems. *Phys. Rev. X* **10**, 031002 (2020).
63. Ku, M. J. H. et al. Imaging viscous flow of the Dirac fluid in graphene. *Nature* **583**, 537–541 (2020).
64. Khanaliloo, B., Mitchell, M., Hryciw, A. C. & Barclay, P. E. High-Q/V monolithic diamond microdisks fabricated with quasi-isotropic etching. *Nano Lett.* **15**, 5131–5136 (2015).
65. Challier, M. et al. Advanced fabrication of single-crystal diamond membranes for quantum technologies. *Micromachines* **9**, 148 (2018).
66. Wood, B. D. et al. Long spin coherence times of nitrogen vacancy centers in milled nanodiamonds. *Phys. Rev. B* **105**, 205401 (2022).
67. Zvi, U. et al. Engineering spin coherence in core–shell diamond nanocrystals. Preprint at https://arxiv.org/abs/2305.03075 (2023).
68. Janitz, E. et al. Diamond surface engineering for molecular sensing with nitrogen-vacancy centers. *J. Mater. Chem. C* **10**, 13533–13569 (2022).
69. Rodgers, L. V. H. et al. Materials challenges for quantum technologies based on color centers in diamond. *MRS Bull.* **46**, 623–633 (2021).

70. Jiang, L. et al. Repetitive readout of a single electronic spin via quantum logic with nuclear spin ancillae. *Science* **326**, 267–272 (2009).
71. Shields, B., Unterreithmeier, Q., De Leon, N., Park, H. & Lukin, M. Efficient readout of a single spin state in diamond via spin-to-charge conversion. *Phys. Rev. Lett.* **114**, 136402 (2015).
72. Hopper, D., Shulevitz, H. & Bassett, L. Spin readout techniques of the nitrogen-vacancy center in diamond. *Micromachines* **9**, 437 (2018).
73. Zhang, Q. et al. High-fidelity single-shot readout of single electron spin in diamond with spin-to-charge conversion. *Nat. Commun.* **12**, 1529 (2021).
74. Irber, D. M. et al. Robust all-optical single-shot readout of nitrogen-vacancy centers in diamond. *Nat. Commun.* **12**, 532 (2021).
75. Degen, C., Reinhard, F. & Cappellaro, P. Quantum sensing. *Rev. Modern Phys.* **89**, 035002 (2017).
76. Arunkumar, N. et al. Quantum logic enhanced sensing in solid-state spin ensembles. *Phys. Rev. Lett.* **131**, 100801 (2023).
77. Zhong, H. et al. Quantitative imaging of exotic antiferromagnetic spin cycloids in $BiFeO_3$ thin films. *Phys. Rev. Appl.* **17**, 044051 (2022).
78. Huxter, W. S. et al. Scanning gradiometry with a single spin quantum magnetometer. *Nat. Commun.* **13**, 3761 (2022).
79. Palm, M. et al. Imaging of submicroampere currents in bilayer graphene using a scanning diamond magnetometer. *Phys. Rev. Appl.* **17**, 054008 (2022).
80. Bar-Gill, N., Pham, L., Jarmola, A., Budker, D. & Walsworth, R. Solid-state electronic spin coherence time approaching one second. *Nat. Commun.* **4**, 1743 (2013).
81. Chang, K., Eichler, A., Rhensius, J., Lorenzelli, L. & Degen, C. L. Nanoscale imaging of current density with a single-spin magnetometer. *Nano Lett.* **17**, 2367–2373 (2017).
82. Ofori-Okai, B. K. et al. Spin properties of very shallow nitrogen vacancy defects in diamond. *Phys. Rev. B* **86**, 081406 (2012).
83. Romach, Y. et al. Spectroscopy of surface-induced noise using shallow spins in diamond. *Phys. Rev. Lett.* **114**, 017601 (2015).
84. Gali, A., Fyta, M. & Kaxiras, E. Ab initio supercell calculations on nitrogen-vacancy center in diamond: electronic structure and hyperfine tensors. *Phys. Rev. B* **77**, 155206 (2008).
85. Gardill, A. et al. Super-resolution airy disk microscopy of individual color centers in diamond. *ACS Photon.* **9**, 3848–3854 (2022).
86. Dolde, F. et al. Room-temperature entanglement between single defect spins in diamond. *Nat. Phys.* **9**, 139–143 (2013).
87. Glenn, D. R. et al. High-resolution magnetic resonance spectroscopy using a solid-state spin sensor. *Nature* **555**, 351–354 (2018).
88. Schmitt, S. et al. Submillihertz magnetic spectroscopy performed with a nanoscale quantum sensor. *Science* **356**, 832–837 (2017).
89. Boss, J. M., Cujia, K. S., Zopes, J. & Degen, C. L. Quantum sensing with arbitrary frequency resolution. *Science* **356**, 837–840 (2017).
90. Joas, T., Waeber, A. M., Braunbeck, G. & Reinhard, F. Quantum sensing of weak radio-frequency signals by pulsed Mollow absorption spectroscopy. *Nat. Commun.* **8**, 964 (2017).
91. Stark, A. et al. Narrow-bandwidth sensing of high-frequency fields with continuous dynamical decoupling. *Nat. Commun.* **8**, 1105 (2017).
92. Meinel, J. et al. Heterodyne sensing of microwaves with a quantum sensor. *Nat. Commun.* **12**, 2737 (2021).
93. Wang, G. et al. Sensing of arbitrary-frequency fields using a quantum mixer. *Phys. Rev. X* **12**, 021061 (2022).
94. Zhang, Z., Joos, M., Bluvstein, D., Lyu, Y. & Bleszynski Jayich, A. C. Reporter-spin-assisted T_1 relaxometry. *Phys. Rev. Appl.* **19**, L031004 (2023).
95. Dubois, A. et al. Untrained physically informed neural network for image reconstruction of magnetic field sources. *Phys. Rev. Appl.* **18**, 064076 (2022).
96. Broadway, D. et al. Improved current density and magnetization reconstruction through vector magnetic field measurements. *Phys. Rev. Appl.* **14**, 024076 (2020).
97. Dovzhenko, Y. et al. Magnetostatic twists in room-temperature skyrmions explored by nitrogen-vacancy center spin texture reconstruction. *Nat. Commun.* **9**, 2712 (2018).
98. Thiel, L. et al. Probing magnetism in 2*d* materials at the nanoscale with single-spin microscopy. *Science* **364**, 973 (2019).
99. Sun, Q.-C. et al. Magnetic domains and domain wall pinning in atomically thin $CrBr_3$ revealed by nanoscale imaging. *Nat. Commun.* **12**, 1989 (2021).
100. Guo, Q. et al. Current-induced switching of thin film α-Fe_2O_3 devices imaged using a scanning single-spin microscope. *Phys. Rev. Mater.* **7**, 064402 (2023).
101. Meisenheimer, P. et al. Switching the spin cycloid in $BiFeO_3$ with an electric field. *Nat. Commun.* **15**, 2903 (2024).
102. Hedrich, N. et al. Nanoscale mechanics of antiferromagnetic domain walls. *Nat. Phys.* **17**, 574 (2021).
103. Hingant, T. et al. Measuring the magnetic moment density in patterned ultrathin ferromagnets with submicrometer resolution. *Phys. Rev. Appl.* **4**, 014003 (2015).
104. Gross, I. et al. Direct measurement of interfacial Dzyaloshinskii–Moriya interaction in *x*|CoFeB|MgO heterostructures with a scanning NV magnetometer (*x* = Ta, TaN, and W). *Phys. Rev. B* **94**, 064413 (2016).
105. Finco, A. et al. Imaging topological defects in a noncollinear antiferromagnet. *Phys. Rev. Lett.* **128**, 187201 (2022).
106. Spaldin, N. A. Analogy between the magnetic dipole moment at the surface of a magnetoelectric and the electric charge at the surface of a ferroelectric. *J. Exp. Theoret. Phys.* **132**, 493–505 (2021).
107. Hubert, A. & Schäfer, R. *Magnetic Domains: The Analysis of Magnetic Microstructures* https://www.springer.com/gp/book/9783540641087 (Springer, 1998).
108. Fert, A., Reyren, N. & Cros, V. Magnetic skyrmions: advances in physics and potential applications. *Nat. Rev. Mater.* **2**, 17031 (2017).
109. Chen, Z. et al. Lorentz electron ptychography for imaging magnetic textures beyond the diffraction limit. *Nat. Nanotechnol.* **17**, 1165–1170 (2022).
110. Marioni, M. A., Penedo, M., Baćani, M., Schwenk, J. & Hug, H. J. Halbach effect at the nanoscale from chiral spin textures. *Nano Lett.* **18**, 2263–2267 (2018).
111. Hrabec, A. et al. Current-induced skyrmion generation and dynamics in symmetric bilayers. *Nat. Commun.* **8**, 15765 (2017).
112. Gross, I. et al. Skyrmion morphology in ultrathin magnetic films. *Phys. Rev. Mater.* **2**, 024406 (2018).
113. Rana, K. G. et al. Room-temperature skyrmions at zero field in exchange-biased ultrathin films. *Phys. Rev. Appl.* **13**, 044079 (2020).
114. Akhtar, W. et al. Current-induced nucleation and dynamics of skyrmions in a co-based Heusler alloy. *Phys. Rev. Appl.* https://doi.org/10.1103/PhysRevApplied.11.034066 (2019).
115. Jenkins, A. et al. Single-spin sensing of domain-wall structure and dynamics in a thin-film skyrmion host. *Phys. Rev. Mater.* **3**, 083801 (2019).
116. Seki, S., Yu, X., Ishiwata, S. & Tokura, Y. Observation of skyrmions in a multiferroic material. *Science* **336**, 198 (2012).
117. Soda, M. et al. Asymmetric slow dynamics of the skyrmion lattice in MnSi. *Nat. Phys.* https://doi.org/10.1038/s41567-023-02120-5 (2023).
118. Psaroudaki, C. & Loss, D. Quantum depinning of a magnetic skyrmion. *Phys. Rev. Lett.* **124**, 097202 (2020).
119. Prozorov, R. & Giannetta, R. W. Magnetic penetration depth in unconventional superconductors. *Superconduct. Sci. Technol.* **19**, R41 (2006).
120. Luan, L. et al. Local measurement of the penetration depth in the pnictide superconductor $Ba(Fe_{0.95}Co_{0.05})_2As_2$. *Phys. Rev. B* **81**, 100501 (2010).
121. Rohner, D. et al. Real-space probing of the local magnetic response of thin-film superconductors using single spin magnetometry. *Sensors* https://doi.org/10.3390/s18113790 (2018).
122. Acosta, V. M. et al. Color centers in diamond as novel probes of superconductivity. *J. Superconduct. Novel Magnet.* **32**, 85 (2019).
123. Borst, M. et al. Observation and control of hybrid spin-wave-Meissner-current transport modes. *Science* **382**, 430–434 (2023).
124. Joshi, K. et al. Measuring the lower critical field of superconductors using nitrogen-vacancy centers in diamond optical magnetometry. *Phys. Rev. Appl.* **11**, 014035 (2019).
125. Kruglyak, V. V., Demokritov, S. O. & Grundler, D. Magnonics. *J. Phys. D: Appl. Phys.* **43**, 264001 (2010).
126. Chen, S. et al. Current induced hidden states in Josephson junctions. *Nat. Commun.* **15**, 8059 (2024).
127. Clem, J. R. Simple model for the vortex core in a type II superconductor. *J. Low Temp. Phys.* **18**, 427 (1975).
128. Loudon, J. C., Yazdi, S., Kasama, T., Zhigadlo, N. D. & Karpinski, J. Measurement of the penetration depth and coherence length of MgB_2 in all directions using transmission electron microscopy. *Phys. Rev. B* **91**, 054505 (2015).
129. Brandt, E. H. Precision Ginzburg–Landau solution of ideal vortex lattices for any induction and symmetry. *Phys. Rev. Lett.* **78**, 2208 (1997).
130. Mao, H.-K., Chen, X.-J., Ding, Y., Li, B. & Wang, L. Solids, liquids, and gases under high pressure. *Rev. Modern Phys.* **90**, 015007 (2018).
131. Acosta, V. M. et al. Color centers in diamond as novel probes of superconductivity. *J. Superconduct. Novel Magnet.* **32**, 85–95 (2019).
132. Kiselev, E. I. & Schmalian, J. Boundary conditions of viscous electron flow. *Phys. Rev. B* **99**, 035430 (2019).
133. Wolf, Y., Aharon-Steinberg, A., Yan, B. & Holder, T. Para-hydrodynamics from weak surface scattering in ultraclean thin flakes. *Nat. Commun.* **14**, 2334 (2023).
134. Balents, L., Dean, C. R., Efetov, D. K. & Young, A. F. Superconductivity and strong correlations in moiré flat bands. *Nat. Phys.* **16**, 725–733 (2020).
135. Kardar, M. *Statistical Physics of Fields* (Cambridge Univ. Press, 2007).
136. Blanter, Y. M. & Büttiker, M. Shot noise in mesoscopic conductors. *Phys. Rep.* **336**, 1–166 (2000).
137. Wang, Y. et al. Shot noise as a characterization of strongly correlated metals. Preprint at https://arxiv.org/abs/2211.11735 (2022).
138. Kobayashi, K. & Hashisaka, M. Shot noise in mesoscopic systems: from single particles to quantum liquids. *J. Phys. Soc. Jap.* **90**, 102001 (2021).
139. Van Der Sar, T., Casola, F., Walsworth, R. & Yacoby, A. Nanometre-scale probing of spin waves using single electron spins. *Nat. Commun.* **6**, 7886 (2015).
140. Wolfe, C. S. et al. Off-resonant manipulation of spins in diamond via precessing magnetization of a proximal ferromagnet. *Phys. Rev. B* **89**, 180406 (2014).
141. Wolfe, C. S. et al. Spatially resolved detection of complex ferromagnetic dynamics using optically detected nitrogen-vacancy spins. *Appl. Phys. Lett.* **108**, 232409 (2016).
142. Wolf, M. S., Badea, R. & Berezovsky, J. Fast nanoscale addressability of nitrogen-vacancy spins via coupling to a dynamic ferromagnetic vortex. *Nat. Commun.* **7**, 11584 (2016).
143. Andrich, P. et al. Long-range spin wave mediated control of defect qubits in nanodiamonds. *npj Quant. Inform.* **3**, 28 (2017).
144. Kikuchi, D. et al. Long-distance excitation of nitrogen-vacancy centers in diamond via surface spin waves. *Appl. Phys. Expr.* **10**, 103004 (2017).
145. Page, M. R. et al. Optically detected ferromagnetic resonance in diverse ferromagnets via nitrogen vacancy centers in diamond. *J. Appl. Phys.* **126**, 124902 (2019).
146. Bertelli, I. et al. Magnetic resonance imaging of spin-wave transport and interference in a magnetic insulator. *Sci. Adv.* **6**, eabd3556 (2020).

147. McCullian, B. A. et al. Broadband multi-magnon relaxometry using a quantum spin sensor for high frequency ferromagnetic dynamics sensing. *Nat. Commun.* **11**, 5229 (2020).
148. Huang, M. et al. Revealing intrinsic domains and fluctuations of moiré magnetism by a wide-field quantum microscope. *Nat. Commun.* **14**, 5259 (2023).
149. Li, S. et al. Observation of stacking engineered magnetic phase transitions within moiré supercells of twisted van der Waals magnets. *Nat. Commun.* **15**, 5712 (2024).
150. Wang, H. et al. Noninvasive measurements of spin transport properties of an antiferromagnetic insulator. *Sci. Adv.* **8**, eabg8562 (2022).
151. Chatterjee, S. et al. Single-spin qubit magnetic spectroscopy of two-dimensional superconductivity. *Phys. Rev. Res.* **4**, L012001 (2022).
152. Dolgirev, P. E. et al. Characterizing two-dimensional superconductivity via nanoscale noise magnetometry with single-spin qubits. *Phys. Rev. B* **105**, 024507 (2022).
153. Flebus, B., Ochoa, H., Upadhyaya, P. & Tserkovnyak, Y. Proposal for dynamic imaging of antiferromagnetic domain wall via quantum-impurity relaxometry. *Phys. Rev. B* **98**, 180409 (2018).
154. Rodriguez-Nieva, J. F. et al. Probing one-dimensional systems via noise magnetometry with single spin qubits. *Phys. Rev. B* **98**, 195433 (2018).
155. Chatterjee, S., Rodriguez-Nieva, J. F. & Demler, E. Diagnosing phases of magnetic insulators via noise magnetometry with spin qubits. *Phys. Rev. B* **99**, 104425 (2019).
156. Khoo, J. Y., Pientka, F., Lee, P. A. & Villadiego, I. S. Probing the quantum noise of the spinon Fermi surface with NV centers. *Phys. Rev. B* **106**, 115108 (2022).
157. Klauder, J. R. & Anderson, P. W. Spectral diffusion decay in spin resonance experiments. *Phys. Rev.* **125**, 912–932 (1962).
158. Savitsky, A., Zhang, J. & Suter, D. Variable bandwidth, high efficiency microwave resonator for control of spin-qubits in nitrogen-vacancy centers. *Rev. Sci. Instrum.* **94**, 023101 (2023).
159. Casanova, J., Wang, Z.-Y., Schwartz, I. & Plenio, M. B. Shaped pulses for energy-efficient high-field NMR at the nanoscale. *Phys. Rev. Appl.* **10**, 044072 (2018).
160. Munuera-Javaloy, C., Tobalina, A. & Casanova, J. High-resolution NMR spectroscopy at large fields with nitrogen vacancy centers. *Phys. Rev. Lett.* **130**, 133603 (2023).
161. Galperin, Y. M., Altshuler, B. L., Bergli, J. & Shantsev, D. V. Non-Gaussian low-frequency noise as a source of qubit decoherence. *Phys. Rev. Lett.* **96**, 097009 (2006).
162. Aslam, N. et al. Quantum sensors for biomedical applications. *Nat. Rev. Phys.* **5**, 157–169 (2023).
163. Lovchinsky, I. et al. Magnetic resonance spectroscopy of an atomically thin material using a single-spin qubit. *Science* **355**, 503–507 (2017).
164. Luan, L. et al. Decoherence imaging of spin ensembles using a scanning single-electron spin in diamond. *Sci. Rep.* **5**, 8119 (2015).
165. Machado, F., Demler, E. A., Yao, N. Y. & Chatterjee, S. Quantum noise spectroscopy of dynamical critical phenomena. *Phys. Rev. Lett.* **131**, 070801 (2023).
166. Ziffer, M. E. et al. Quantum noise spectroscopy of critical slowing down in an atomically thin magnet. Preprint at https://arxiv.org/abs/2407.05614 (2024).
167. Ji, W. et al. Correlated sensing with a solid-state quantum multisensor system for atomic-scale structural analysis. *Nat. Photon.* https://www.nature.com/articles/s41566-023-01352-4 (2024).
168. Delord, T., Monge, R. & Meriles, C. A. Correlated spectroscopy of electric noise with color center clusters. *Nano Lett.* **24**, 6474–6479 (2024).
169. Broholm, C. et al. Quantum spin liquids. *Science* **367**, eaay0668 (2020).
170. Wörnle, M. S. et al. Coexistence of Bloch and Néel walls in a collinear antiferromagnet. *Phys. Rev. B* **103**, 094426 (2021).
171. Meisenheimer, P., Moore, G., Zhou, S. et al. Switching the spin cycloid in $BiFeO_3$ with an electric field. *Nat. Commun.* **15**, 2903 (2024).
172. Belashchenko, K. D. Equilibrium magnetization at the boundary of a magnetoelectric antiferromagnet. *Phys. Rev. Lett.* **105**, 147204 (2010).
173. Moriya, T. Anisotropic superexchange interaction and weak ferromagnetism. *Phys. Rev.* **120**, 91–98 (1960).
174. Andreev, A. F. Macroscopic magnetic fields of antiferromagnets. *J. Exp. Theoret. Phys. Lett.* **63**, 758–762 (1996).
175. Jiang, K. et al. Kagome superconductors *A*V3Sb5 (*A* = K, Rb, Cs). *Natl Sci. Rev.* **10**, nwac199 (2023).
176. Xia, J., Maeno, Y., Beyersdorf, P. T., Fejer, M. M. & Kapitulnik, A. High resolution polar Kerr effect measurements of Sr_2RuO_4: evidence for broken time-reversal symmetry in the superconducting state. *Phys. Rev. Lett.* **97**, 167002 (2006).
177. Haldane, F. D. M. Model for a quantum hall effect without Landau levels: condensed-matter realization of the 'parity anomaly'. *Phys. Rev. Lett.* **61**, 2015–2018 (1988).
178. Tschirhart, C. L. et al. Imaging orbital ferromagnetism in a moiré Chern insulator. *Science* **372**, 1323–1327 (2021).
179. Sacépé, B., Feigel'man, M. & Klapwijk, T. M. Quantum breakdown of superconductivity in low-dimensional materials. *Nat. Phys.* **16**, 734–746 (2020).
180. Hayden, S. M. & Tranquada, J. M. Charge correlations in cuprate superconductors. *Annu. Rev. Condens. Matter Phys.* **15**, 032922–094430 (2024).
181. He, F. et al. Moiré patterns in 2D materials: a review. *ACS Nano* **15**, 5944–5958 (2021).
182. Abrahams, E., Kravchenko, S. V. & Sarachik, M. P. Metallic behavior and related phenomena in two dimensions. *Rev. Modern Phys.* **73**, 251–266 (2001).
183. Spivak, B. & Kivelson, S. A. Phases intermediate between a two-dimensional electron liquid and Wigner crystal. *Phys. Rev. B* **70**, 155114 (2004).
184. Ahn, S. & Das Sarma, S. Density-tuned effective metal–insulator transitions in two-dimensional semiconductor layers: Anderson localization or Wigner crystallization. *Phys. Rev. B* **107**, 195435 (2023).
185. Sung, J. et al. Observation of an electronic microemulsion phase emerging from a quantum crystal-to-liquid transition. Preprint at http://arxiv.org/abs/2311.18069 (2023).
186. Nie, L., Tarjus, G. & Kivelson, S. A. Quenched disorder and vestigial nematicity in the pseudogap regime of the cuprates. *Proc. Natl Acad. Sci. USA* **111**, 7980–7985 (2014).
187. Vojta, T. Disorder in quantum many-body systems. *Annu. Rev. Condens. Matter Phys.* **10**, 233–252 (2019).
188. Mitra, A., Takei, S., Kim, Y. B. & Millis, A. J. Nonequilibrium quantum criticality in open electronic systems. *Phys. Rev. Lett.* **97**, 236808 (2006).
189. Green, A. G., Moore, J. E., Sondhi, S. L. & Vishwanath, A. Current noise in the vicinity of the 2D superconductor-insulator quantum critical point. *Phys. Rev. Lett.* **97**, 227003 (2006).
190. Cavalleri, A. Photo-induced superconductivity. *Contemp. Phys.* **59**, 31–46 (2018).
191. Dolde, F. et al. Electric-field sensing using single diamond spins. *Nat. Phys.* **7**, 459–463 (2011).
192. Neumann, P. et al. High-precision nanoscale temperature sensing using single defects in diamond. *Nano Lett.* **13**, 2738–2742 (2013).
193. Doherty, M. W. et al. Electronic properties and metrology applications of the diamond NV-center under pressure. *Phys. Rev. Lett.* **112**, 047601 (2014).
194. Franz, R. & Wiedemann, G. Ueber die Wärme–Leitungsfähigkeit der Metalle. *Annalen der Physik* **165**, 497–531 (1853).
195. Waissman, J. et al. Electronic thermal transport measurement in low-dimensional materials with graphene non-local noise thermometry. *Nat. Nanotechnol.* **17**, 166–173 (2022).
196. Tang, J. et al. Quantum diamond microscope for dynamic imaging of magnetic fields. *AVS Quant. Sci.* **5**, 044403 (2023).
197. Barry, J. F. et al. Sensitive AC and DC magnetometry with nitrogen-vacancy center ensembles in diamond. Preprint at https://arxiv.org/abs/2305.06269 (2023).
198. Waxman, A. et al. Diamond magnetometry of superconducting thin films. *Phys. Rev. B* **89**, 054509 (2014).
199. Liu, K. S. et al. Surface NMR using quantum sensors in diamond. *Proc. Natl Acad. Sci. USA* **119**, e2111607119 (2022).
200. Rodgers, L. V. H. et al. Diamond surface functionalization via visible light-driven C-H activation for nanoscale quantum sensing. *Proc. Natl Acad. Sci. USA* **121**, e2316032121 (2024).
201. Bian, K. et al. Nanoscale electric-field imaging based on a quantum sensor and its charge-state control under ambient condition. *Nat. Commun.* **12**, 2457 (2021).
202. Chen, E. H. et al. High-sensitivity spin-based electrometry with an ensemble of nitrogen-vacancy centers in diamond. *Phys. Rev. A* **95**, 053417 (2017).
203. Qiu, Z., Hamo, A., Vool, U., Zhou, T. X. & Yacoby, A. Nanoscale electric field imaging with an ambient scanning quantum sensor microscope. *npj Quant. Inform.* **8**, 107 (2022).
204. Huxter, W. S., Sarott, M. F., Trassin, M. & Degen, C. L. Imaging ferroelectric domains with a single-spin scanning quantum sensor. *Nat. Phys.* **19**, 644–648 (2023).
205. Michl, J. et al. Robust and accurate electric field sensing with solid state spin ensembles. *Nano Lett.* **19**, 4904–4910 (2019).
206. Marshall, M. C. et al. High-precision mapping of diamond crystal strain using quantum interferometry. *Phys. Rev. Appl.* **17**, 024041 (2022).
207. Wang, J. et al. High-sensitivity temperature sensing using an implanted single nitrogen-vacancy center array in diamond. *Phys. Rev. B* **91**, 155404 (2015).
208. Shim, J. H. et al. Multiplexed sensing of magnetic field and temperature in real time using a nitrogen-vacancy ensemble in diamond. *Phys. Rev. Appl.* **17**, 014009 (2022).
209. Moreva, E. et al. Practical applications of quantum sensing: a simple method to enhance the sensitivity of nitrogen-vacancy-based temperature sensors. *Phys. Rev. Appl.* **13**, 054057 (2020).
210. Cambria, M. et al. Temperature-dependent spin-lattice relaxation of the nitrogen-vacancy spin triplet in diamond. *Phys. Rev. Lett.* **130**, 256903 (2023).
211. Ernst, S., Scheidegger, P. J., Diesch, S. & Degen, C. L. Modeling temperature-dependent population dynamics in the excited state of the nitrogen-vacancy center in diamond. *Phys. Rev. B* **108**, 085203 (2023).
212. Happacher, J. et al. Temperature-dependent photophysics of single NV centers in diamond. *Phys. Rev. Lett.* **131**, 086904 (2023).
213. Bauch, E. et al. Decoherence of ensembles of nitrogen-vacancy centers in diamond. *Phys. Rev. B* **102**, 134210 (2020).
214. Jarmola, A. et al. Longitudinal spin-relaxation in nitrogen-vacancy centers in electron irradiated diamond. *Appl. Phys. Lett.* **107**, 242403 (2015).
215. Choi, J. et al. Depolarization dynamics in a strongly interacting solid-state spin ensemble. *Phys. Rev. Lett.* **118**, 093601 (2017).
216. Myers, B. A. et al. Probing surface noise with depth-calibrated spins in diamond. *Phys. Rev. Lett.* **113**, 027602 (2014).
217. Barson, M. S. J. et al. Nanomechanical sensing using spins in diamond. *Nano Lett.* **17**, 1496–1503 (2017).
218. Myers, B., Ariyaratne, A. & Jayich, A. B. Double-quantum spin-relaxation limits to coherence of near-surface nitrogen-vacancy centers. *Phys. Rev. Lett.* **118**, 197201 (2017).
219. Langsjoen, L. S., Poudel, A., Vavilov, M. G. & Joynt, R. Qubit relaxation from evanescent-wave Johnson noise. *Phys. Rev. A* **86**, 010301 (2012).
220. Fang, H., Zhang, S. & Tserkovnyak, Y. Generalized model of magnon kinetics and subgap magnetic noise. *Phys. Rev. B* **105**, 184406 (2022).

221. Lovchinsky, I. et al. Nuclear magnetic resonance detection and spectroscopy of single proteins using quantum logic. *Science* **351**, 836–841 (2016).
222. Pham, L. M. et al. NMR technique for determining the depth of shallow nitrogen-vacancy centers in diamond. *Phys. Rev. B* **93**, 045425 (2016).

Acknowledgements
The authors acknowledge helpful discussions with S. Kolkowitz, L. Jiang, A. Yazdani, P. Dolgirev, P. Armitage, J. Marino, A. Imamoglu, M. Lukin, H. Hosseinabadi, A. Yacoby and N. Yao. This work was supported by the National Science Foundation (QuSEC-TAQS OSI 2326767 and Princeton University's Materials Research Science and Engineering Center DMR-2011750) (N.P.d.L. and S.G.); the Gordon and Betty Moore Foundation (grant DOI 10.37807/gbmf12237) (N.P.d.L.); the Intelligence Community Postdoctoral Research Fellowship Program by the Oak Ridge Institute for Science and Education (ORISE) through an interagency agreement between the US Department of Energy and the Office of the Director of National Intelligence (ODNI) (J.R.); the European Research Council's grant 'QS2DM' and from the Swiss National Science Foundation through Project 188521 (P.M.); the Gordon and Betty Moore Foundation's EPiQS Initiative via Grant GBMF10279 and the DOE QNEXT (A.C.B.J.); the DOE Q-NEXT Center (Grant number DOE 1F-60579) (A.C.B.J.); the SNSF project (200021-212899) and the Swiss State Secretariat for Education, Research and Innovation (contract number UeM019-1).

Author contributions
All authors contributed equally to this manuscript.

Competing interests
The authors declare no competing interests.

Additional information
Peer review information *Nature Reviews Physics* thanks Toeno van der Sar and the other, anonymous, reviewer(s) for their contribution to the peer review of this work.

Publisher's note Springer Nature remains neutral with regard to jurisdictional claims in published maps and institutional affiliations.

Springer Nature or its licensor (e.g. a society or other partner) holds exclusive rights to this article under a publishing agreement with the author(s) or other rightsholder(s); author self-archiving of the accepted manuscript version of this article is solely governed by the terms of such publishing agreement and applicable law.

© Springer Nature Limited 2024